Nucleation processes in porous media:

Method development and experimental study of frost damage in trees

by
Even Sogn Andersen

Thesis for the degree of Master of Science

Department of Physics

Faculty of Mathematics and Natural Sciences

University of Oslo

July 2012

Acknowledgement

I would like to thank my supervisors Dag Kristian Dysthe and Anja Røyne for their continued help and encouragement. Without their insights and willingness to help, I would probably still be sitting in the lab twiddeling my thumbs. The same can be said for Olav Gundersen, who was a great help in both developing the software and making the ring LED light used in the experiments. Also, he is a great telemark ski instructor.

I also want to thank my parents, Arve and Wivi, for their moral support and the occasinal hot meal. That might be worth more to a starving student than many people realize.

Lastly, I would like to thank my sisters, Guri, Mari and Marte, and my friends Øystein, Marie, Matthew, Audun, Nils, Henrik, Nick and Per-Anders for their uplifting words and patience in listening to the phyics ramblings of a master student.

Contents

Chapter 1

Introduction

1.1 Background

In nature, trees have the ability to filter water through the root membrane and pull relatively clean water from the ground and transport it all the way up to the canopy. This process is driven by water evaporation from the leaves, which creates a pressure gradient with lower, and often negative, pressure in the canopy and higher pressures further down. The xylem is the water conducting tissue mostly found in vascular plants such as conifers and angiosperms. The tissue contains hollow cells called tracheids, and it is through them that water is transported along the negative pressure gradient, i.e. from the roots to the leaves, as shown in figure 1.1.

The tracheids constitute a network of pipe-like structures that is made up of dead cells [Hacke and Sperry, 2001]. Since the work needed to drive water transportation is done by the passive evaporation from the leaves, there is no need for the cells to produce adenosine triphosphate (ATP) and no need for a an active cell nucleus. This allows the cells to adopt a structure which maximizes fluid flow. The diameter of individual tracheids in conifers typically ranges from $5 - 500\mu$m, and they can be from a few mm up to 10m long. The tracheids taper at the ends and are connected through pit openings where one typically finds a porous pit membrane. This membrane acts to impede intruding air from embolizing other tracheids in case of damage, but they allow for fluid flow. To keep the conduits from collapsing under negative pressure, the cells usually need additional support from a lignified matrix, however some xylem cells are strong enough to act as support on their own. The latter is typical for conifer stem wood [Hacke and Sperry, 2001].

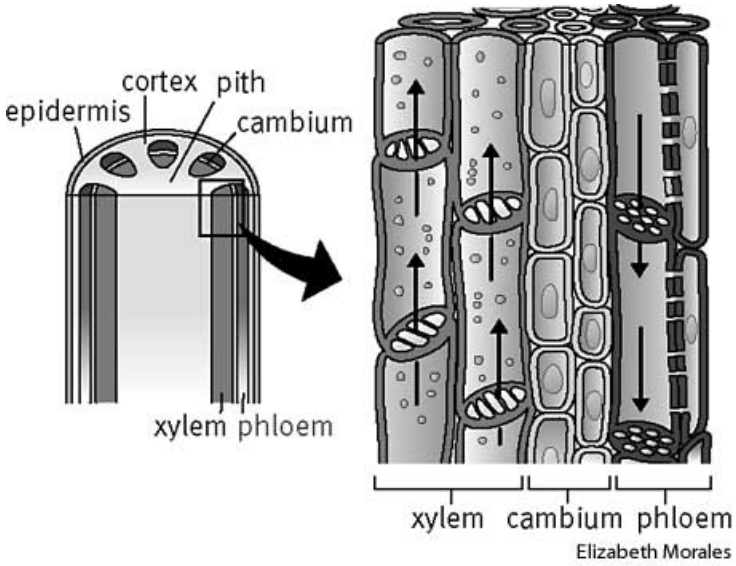

Figure 1.1: A schematic of the xylem tissue of trees which transport water from the root to the leaves through the tracheids. (Picture taken from http://images.yourdictionary.com/xylem)

The in situ pressure in leaves has been measured to be as low as -10MPa, which, so far, superceeds any mechanical pump that allows for net flow or synthetic wick mechanism produced today [Wheeler and Stroock, 2008]. As a comparison, the atmospheric pressure at the earth surface is ≈ 0.1MPa. Liquid water that is not subject to confinement becomes unstable with respect to its vapor phase when the pressure becomes negative. Water that stays liquid under tensile forces of this magnitude, as in the xylem, is in reality in a metastable equilibrium, so if the pressure drops beyond a critical value, the system might undergo a phase change and start to nucleate gas bubbles. This is often referred to as cavitation and it is believed to be one of the dominant mechanisms for the formation of embolisms in trees. The gas can be either dissolved air in the water which is forced out of solution or it can be water vapor. The latter can happen if the water does no contain dissolved gas. However, the water in trees generally contain some dissolved gas and it is this gas that typically form embolisms.

During draught, trees can experience increased negative pressures due to a combination of the lack of refilling from the roots and the dry air which increases evaporation from the canopy. In this case, the negative pressure might become large enough to vaporize water to create water vapor embolims. If one tracheid nucleates a gas bubble and embolizes, the volume of gas might

expand to other tracheids through the pit openings that connect individual tracheid cells. The maximum pressure that can be sustained by a circular opening (pit opening) is determined by the pit radius, since

$$\Delta P = \frac{2\sigma \cos(\alpha)}{r_p} \tag{1.1}$$

where σ is the surface tension of water, α is the contact angle between the meniscus and the cell wall and r_p is the radius of the pit opening [Hacke and Sperry, 2001]. In addition, some trees have pit openings that are covered with a porous pit membrane. This membrane allows for fluid flow, but it significantly decreases r_p, allowing for larger ΔP. The pit membranes thus act as check valves which allow for fluid flow, but restrict the expansion of potential embolsisms between tracheids.

An experiment was conducted by Wheeler and Stroock [2008] to create a synthetic tree. The idea was to recreate the trees ability to create such low pressures. In order to create a synthetic tree, they needed a material to act as the semipermeable membranes found in the roots and leaves of trees. The material used in this study was a hydrogel which was cast on a mold made using a soft photolithography technique. This allowed the authors to create a microfluidic network with one part acting as the leaves and one part acting as the roots. These parts were connected with a thin channel representing the xylem in the trunk. Further, the "root" was subjected to water and the "leaves" to evaporation, thus simulating a tree's mechanism for water transportation.

For natural trees, it has been suggested that when the root absorbs water by reversed osmosis which suggests that the water in the tree is relatively free from impurities and therefore less susceptible to cavitation. Still, when Wheeler and Stroock [2008] punctured the root membrane and allowed for a direct inlet of water in their system, they managed to produce a pressure in the synthetic leaves of $P_{leaf} = -1.0$MPa which is fifteen-fold greater in magnitude than any synthetic pumping system [Wheeler and Stroock, 2008].

The nucleation of gas bubbles in the tracheids of trees is believed to be one of the main causes of frost damage. The hypothesis, often referred to as the thaw-expansion hypothesis [Mayr and Sperry, 2010], is that when the water in the xylem freezes, the gas that was dissolved in the water is separated out due to the low solubility of gas in ice. These bubbles are trapped in the ice. On thawing, these bubbles might redissolve, if they are small enough, or grow to form an embolism due to the low pressures caused by evaporation of water in the canopy.

The work of Mayr et al. [2003] has shed light on this phenomenon. Previous to this study, there were inconsistencies between the findings in field studies and experimental work, namely that field work showed naturally occuring examples of frost damage to conifers while the experimental studies showed that conifers were resistant to frost damage. Mayr et al. [2003] suggested that draught stress might be a contributing factor to frost damage which could explain the discrepany. To test the hypothesis, experiments were conducted by taking potted specimens of Norway spruce and stone pine and drying them to various extents. This allowed them to control the xylem pressure and simulate conditions when a tree is subjected to draught. The samples were then exposed to freeze-thaw cycles in a temperature chamber with freezing and thawing rates as well as temperatures corresponding to conditions measured in Tyrol (Central Alps). One batch of trees went through 50 freeze-thaw cycles and another went through 100 cycles. One control batch of trees was not subjected to freeze-thaw cycles.

As a measure of the amount om embolized tracheids, the percentage loss of conductivity was used. When Mayr et al. [2003] compared the percentage loss of water conductivity, they noted that for both tree types (Norway spruce and stone pine), the embolism rates were significantly higher for trees that had undergone more cycles. The pressure corresponding to 50% loss of conductivity for the three batches (0, 50 and 100 cycles) was measured. This pressure, for the batch that went through 100 cycles, was found to be displaced by as much as 1.8MPa and 0.8MPa for Norway spruce and stone pine respectively. This tells us that when increasing the number of cycles, less draught stress (less negative xylem pressure) is needed to induce a 50% loss of water conductivity. In other words, the results imply that the number of embolisms in trees increases with the number of freeze-thaw cycles. The difference between the two species was explained by the fact that Norway spruce has wider tracheids than stone pine. This structural difference makes it more vulnerable to freeze-thaw induced embolisms due to bigger volumes of water, and therefore dissolved gas, in each tracheid.

The study showed that the mismatch between earlier experimental work and field studies could be explained by the fact that trees in nature are exposed to several freeze-thaw cycles which, in combination with draught, greatly affects the formation of embolisms. However, the study did not determine why several cycles induced more embolisms.

Another experimental study was conducted by Mayr and Sperry [2010], in which stem samples were cut from trees of the species Pinus contorta. The samples were saturated with water such that the initial xylem pressure would

be equal for all samples. During the experiments a centrifuge with a temperature control function was used to control the xylem pressure, freezing and thawing rates and maximum and minimum temperature. The loss of water conductivity was measured using the same method as in Mayr et al. [2003].

As a control referance, stems were spun such that the pressure was $P = -3$MPa without subjecting them to freeze-thaw cycling. It was found that the precentage loss of conductivity (PLC) was $4.4 \pm 1.2\%$ and that the duration of the experiment did not influence the PLC. However, when subjected to one freeze-thaw cycle at the same pressure, the PLC was $32.2 \pm 4.0\%$. Similar results were found using pressures during freezing of -0.5MPa and -3MPa during thawing ($35.2 \pm 4.3\%$). In the opposite case, when $P = -3$MPa on freezing and $P = -0.5$MPa on thawing, a PLC of only $6.7 \pm 1.9\%$ was found. In addition, the effects of the minimum temperature was tested on the control samples and no effect on the PLC was found. Mayr and Sperry [2010] also reported that when stems were subjected to two cycles, the PLC increased considerably ($49.8 \pm 4.0\%$).

This tells us that it was the pressure during thawing that was crucial to the loss of conductivity which is in agreement with the thaw-expansion hypothesis. They also found that two cycles increases the PLC compared to one cycle, which is in agreement with the results in Mayr et al. [2003]. On the subject of the effect of repeated freeze-thaw cycles, Mayr and Sperry [2010] stated that it has been suggested that the cavitation event could be subject to some degree of stochasticity. Another possibility being that cavitation in one tracheid increases the pressure in neighbouring tracheids and thus reduces the probability of cavitation there. This is still an open question.

In summation, we observe that embolisms in trees are formed on thawing of ice and that the pressure on thawing is a key factor for the amount of embolized material formed. This is explained by the freeze thaw hypothesis. The aspect that is not explained is why repeated freeze thaw cycles induce more embolisms.

1.2 The aim of the thesis

Even though both Mayr et al. [2003], Mayr and Sperry [2010] find evidence that supports the freeze thaw hypothesis, they do not observe the process directly. Further, they do not explain why repeated freeze thaw cycles induce more embolisms. The mechanisms behind this effect will be the focus of this

thesis.

The initial idea was to observe the release of gas during thawing directly to observe whether gas is released over consecutive cycles or if all dissolved gas is separated out during the first cycle. If gas is released over many cycles, it might help explain the effect shown in Mayr et al. [2003], Mayr and Sperry [2010] where they observed an increased embolism rate with increased number of cycles, the idea being that there was some stochasticity to the size of the bubbles released each time it thawed. This could indicate that some bubbles might become large enough to cavitate even after the first cycle.

The aim of this thesis has been to develop a method by combining the experimental techniques of Mayr et al. [2003], Mayr and Sperry [2010], Wheeler and Stroock [2008] to study a microfluidic network during repeated freeze thaw cycles. Using this method, both the freezing process and the nucleation of gas bubbles were observed directly.

Chapter 2

Theory

In this chapter the basic thermodynamics of nucleation will be presented and discussed in context with the type of porous systems used to study nucleation. Before proceeding it is worth mentioning that the existing literature often uses a different statistical ensemble than what most of the derivations here will be based on. In this thesis, the derivations are mainly based on the work done in Feder [1996] where he utilized the grand canonical ensemble with the corresponding Landau potential, or grand potetential. Other authors [Mullin, 2001, Lasaga, 1998] used the canonical ensemble with the Gibbs free energy, or canonical potential. The end result is equivalent.

Using the grand canonical ensemble, the reversible work done producing a new phase given that V, μ and T are constant is equal to the change in the grand potential. Had we instead chosen our ensemble to model a system where we held P, N and T fixed, we would be in the canonical ensemble.

2.1 Thermodynamics of nucleation

Nucleation is the event where a thermodynamically stable cluster, or nucleus, is formed during a phase transformation. The driving mechanism for such a process is the minimization of free energy of the system by going from solid to liquid, liquid to gas etc.

The newly formed stable cluster is normally too small to observe directly, but we see the consequence of the nucleation process every day. When a kettle boils, the water vapor bubbles we see started out as tiny clusters of water molecules in the gaseous phase that became stable and continued to

grow into macroscopic sized bubbles. The driving force behind the process is simply that at temperatures over 100°C at 1atm pressure, the gas phase of water has a lower energy than that of liquid water, i.e. the kettle of liquid water is trying to minimize its energy.

Now, some key aspects of the thermodynamics of nucleation will be discussed before taking a broader view on how this theory applies to the real world.

2.2 Surface energy

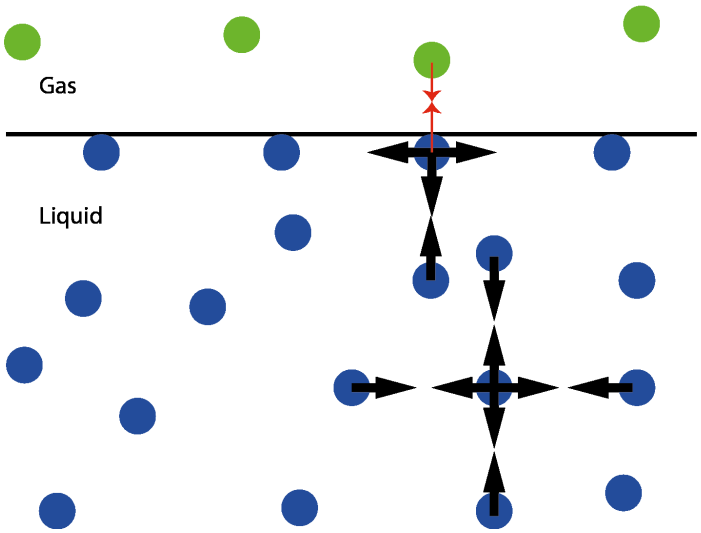

Figure 2.1: A schematic view of how atoms on a surface has fewer atoms to interact with than those of the bulk. The weaker the interaction across the interface gets, the higher the surface energy is.

Qualitatively speaking, the surface energy, σ, is the energy associated with one unit of surface. It is a consequence of the fact that the atoms on a surface have fewer atoms to interact with than the bulk atoms, as shown in figure 2.1. The particles on the surface have less than, or equal to, half as many neighbouring particles to interact with, so if the particles of the bulk have an interaction energy, U, then particles on the surface have an interaction energy of approximately $U/2$. This difference is exactly what we observe as surface energy, or surface tension. This means that if a system needs to minimize its energy, it can adopt the configuration of surfaces with the lowest energy cost.

In figure 2.1 we see that the particles on the surface interact weakly (small red arrows) across the surface. This interaction leads to a slightly lower difference in interaction energy between bulk and surface particles than if the interaction was absent and hence a lower surface energy when two media are in contact. The particles on either side of the interface can also interact by repelling each other, causing an even higher surface energy than in the case of no interaction.

Although the effect of surface energy is more easily observed for a liquid, it is also present in a solid. As for a liquid, the atoms on the surface of a solid have a different interaction energy than that of the bulk, but due to the rigidity of normal solids the effect is not as obvious. Consider a solid in a vacuum. If one does reversible work on it by cutting it in half, the work done is equal to the energy of the two new surfaces created.

Let us now consider two bodies in contact with an interfacial area equal to A, e.g. a drop of fluid in another fluid or gas. If we do reversible work on the system by altering the contact area by an amount, δA, but keep both volumes constant, we will have done work equal to

$$\delta W = \sigma \delta A \tag{2.1}$$

One possibility would be to change the shape of a droplet from a sphere to an ellipsoid with the same volume. Note that if $\frac{\delta W}{\delta A}$ is negative, σ is negative. If this is the case, the system could lower its energy by doing negative work by increasing the interface between the two bodies, i.e. they would mix.

If we now consider the attractive forces of the interactions, see the black arrows in Figure 2.1, the atoms of the bulk are pulled equally in every direction giving each particle a net force equal to zero. On the surface, however, the net force points away from the surface and towards the bulk. This means that the net force acting on the surface particles sets up a pressure which allows the surface to withstand some external force without "breaking". This effect is easily observed by watching certain bugs, like the aptly named water strider, walk on water or seeing a paper clip floating in a cup. The cause behind this effect will now be derived using thermodynamics.

2.2.1 The Young-Laplace law

A drop of fluid (l) with radius R is surrounded by a gas (g) as shown in figure 2.2. At a given temperature, T, and chemical potential, μ, the system has a

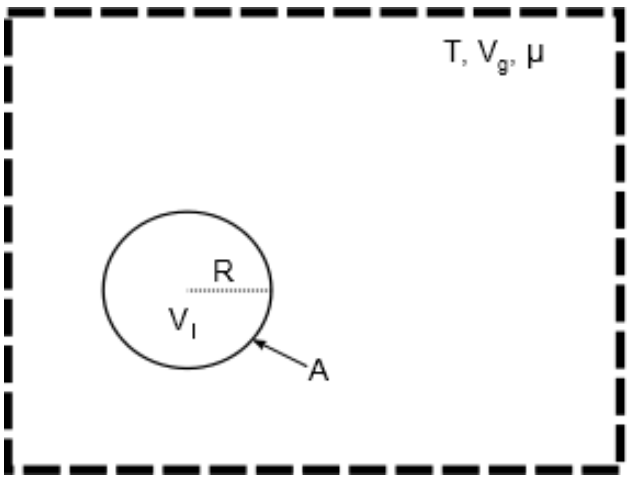

Figure 2.2: A drop of liquid with volume V_l, area A at fixed temperature and chemical potential. The drop is surrounded by vapor of the same composition.

potential energy

$$\Omega = -P_l V_l - P_g V_g + \sigma A. \tag{2.2}$$

We know that $V = V_l + V_g$, so this allows us to rewrite the expression as

$$\Omega = -P_l V_l - P_g(V - V_l) + \sigma A. \tag{2.3}$$

Assuming a spherical droplet, we can insert the appropriate geometrical functions for the volume $V_l = \frac{4}{3}\pi R^3$ and contact area $A = 4\pi R^2$. A small change in radius then gives

$$\delta\Omega = \left(\frac{\delta\Omega}{\delta R}\right)_{T,\mu,V} \delta R = [-(P_l - P_g)4\pi R^2 + \sigma 8\pi R]\delta R \tag{2.4}$$

Solving this for equilibrium, $\delta\Omega = 0$, gives the Young-Laplace equation

$$P_l - P_g = \frac{2\sigma}{R} \tag{2.5}$$

Because the surface energy must be strictly positive to achieve equilibrium between two phases, the left hand side of equation 2.5 must also be positive. This tells us that the pressure inside the drop is larger than the vapor pressure surrounding it, and that it is a function of the radius or curvature.

There are also other ways of deriving this expression. One example, using a mechanical approach, was done by Feder [1996]. He considered an interacting

potential between molecules which had a finite length and integrated over all possible interactions between two sides of a separated liquid. In this case, the surface energy can be found when the two separated bodies are so far away that the molecules on one side do not interact with molecules in the other.

2.3 Nucleation

In the previous section we discussed an equilibrium situation, but nucleation is a process that takes place in a system out of equilibrium. It is a process where molecules collide at random, and some molecules end up sticking together forming small clusters. In reality, this happens all the time due to fluctuations, but if the system is in equilibrium, the thermodynamical potential will not be lowered by the formation of stable nuclei, and the cluster simply dissolves or evaporates. Given the right conditions, the formation of a stable nucleus may lower the thermodynamic potential of the system. If this is the case, nucleation will generally be favored.

Imagine a system similar to that shown in Figure 2.2, but this time the system is not in equilibrium and the radius is allowed to vary. Given that the system is large enough ($V_g \gg V_l$), we can consider $P_g = P$ to be fixed. Before the formation of a small cluster the grand potential is $\Omega = -PV$, but when a cluster forms the potential is $\Omega = -P(V - V_l) - P_l V_l + \sigma A$. Therefore, the change in potential, which is the same as the reversible work done to produce the cluster, W, is given by

$$W = \Delta\Omega = -(P_l - P)V_l + \sigma A \tag{2.6}$$

Inserting expressions for the volume and area given a spherical droplet of radius R yields

$$W = \Delta\Omega = -\frac{4\pi(P_l - P)}{3}R^3 + 4\pi\sigma R^2 \tag{2.7}$$

This expression can be made dimensionless. If we study equation 2.7, we see that the first term is negative due to the fact that P_l is larger than P due to the surface tension, as we showed when deriving the Young-Laplace law (equation 2.5). Also, the second term is strictly positive because $\sigma > 0$. This tells us that the amount of reversible work needed to create clusters of size R will reach a peak value where

$$\frac{dW}{dR} = \frac{d\Delta\Omega}{dR} = 0 \tag{2.8}$$

If we solve this for R, we get the critical radius, R^*,

$$R^* = \frac{2\sigma}{P_l - P} \tag{2.9}$$

and inserting this back into equation 2.7 we obtain the peak value often referred to as the energy barrier (or just barrier) to nucleation, W^*:

$$W^* = \Delta\Omega^* = \frac{4}{3}\pi\sigma R^{*2} = \frac{16\pi}{3}\frac{\sigma^3}{(P_l - P)^2} \tag{2.10}$$

Equation 2.7 can be made dimensionless by dividing W by W^*, which after some manipulation yields the function plotted in figure 2.3:

$$\frac{W}{W^*} = -2\left(\frac{R}{R^*}\right)^3 + 3\left(\frac{R}{R^*}\right)^2 \tag{2.11}$$

Note that this expression is exactly the same as we would have gotten if we started out using the canonical ensemble with the Gibbs free energy.

We know that in order for the system to lower its potential energy, $\Delta\Omega$ must be negative. If it is negative, it means that the system does negative work when creating clusters. In addition, we have assumed that the system started out without any existing clusters and that the cluster growth effectively happens by monomer attachment and detachment. Qualitatively, the latter means that two large clusters cannot collide and create one very large cluster. The reason for this is that the probability of such a process is exceedingly low. Instead, it must grow with a "continuous" radius. With this in mind, the peak value, W^*, represents the minimum work which must be available to the system in order to reach cluster sizes that correspond to negative $\Delta\Omega$. This is what is often referred to as the barrier to nucleation, and in most systems the work required to cross this barrier is provided by fluctuations of thermodynamic quantities, typically temperature, pressure, density and so on.

Essentially, if all the fluctuations in the system are smaller than this barrier, they will not be able to provide the necessary work to create clusters large enough to be stable, that is, clusters larger than R^*. However, if the fluctuations are big enough to provide the work needed to overcome the barrier, there is nothing to keep the system from creating larger clusters that continue to grow. In this scenario, the system minimizes its potential by preforming work, i.e. creating stable nuclei.

These calculations can be done for a similar system where we instead of a drop of liquid in gas have a bubble of gas in a liquid. The calculations,

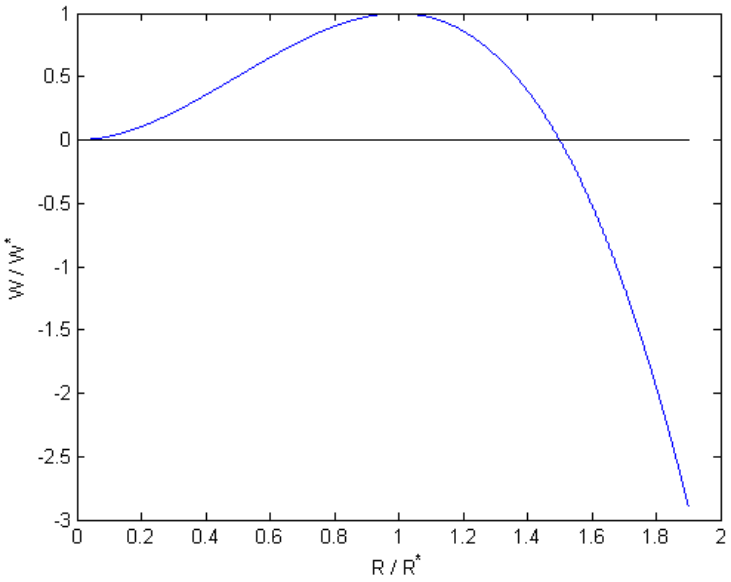

Figure 2.3: A dimensionless plot of the work required to create a cluster of size R. The function plotted is equation 2.11. The black line shows where $\frac{W}{W^*} = 0$

assumptions and results are equivalent, and the major difference is that the controlling parameters must be such that nucleation of gas is favoured in this system. In the system described above, one can think of the drop of liquid in a gas as liquid water condensing from a large volume of water vapor. The latter case, with the bubble of gas, can be a large volume of liquid water when it starts to nucleate water vapor, i.e. it boils. The controlling parameter can be the temperature, which determines, at constant pressure, which phase that is favoured.

Something that should be pointed out before continuing is that if we consider the potential energy of a system, we must imagine its possible values as lying on a surface in a multidimensional phase space. This means that if one wishes to go from one value of the potential energy to another, there are in theory an infinite number of possible routes to take. Naturally, most of these are unlikely to a point where they can be ignored and this is exactly what the derivations above are based on. The point is that the barrier described above is the one that requires the least amount of work to overcome. It is a simplification that is used to keep the math and physics manageable. In essence, other paths are available to the system, but they are highly unlikely.

2.3.1 Homogeneous & heterogeneous nucleation

In the previous section nucleation in the general sense was discussed, but much of the literature refers to two distinct "types" of nucleation. One is homogeneous nucleation where one assumes an ideal system without impurities or irregular geometries. Heterogeneous nucleation is what commonly occurs in nature where nucleation is aided by impurities or geometries which act as centers for nucleation. They effectively lower the barrier to nucleation on the surfaces that they are in contact with or offer a geometry that allows the nucleus to have a lower surface-to-volume ratio, i.e. the amount of work needed to grow large stable clusters is lowered.

In reality, the theory for describing both processes is the same. However, for heterogeneous nucleation, one must take into consideration several interfaces with different surface energies and possible geometries that are energetically favourable. Nucleation is most likely to occur on the surface with the lowest barrier to nucleation.

When evaluating σ, one must consider that in real systems the actual value is not simply the energy needed to form a surface, but an interface! If there exists surfaces that could allow for a lower interfacial energy it means that the amount of work needed to nucleate there is less, and therefore one does not need fluctuations to be as high as they would need to be in the absence of such surfaces. This is the effect you can observe when superheating pure water in a microwave. The water remains liquid above 100°C, but if you introduce an impurity, such as a sugar cube, the barrier to nucleation is lowered and it instantly starts nucleation gas, i.e. it boils. It is the same principle which allows you to create a cola vulcano by putting menthos into the bottle. The following section will consider what happens to the energetics when we introduce a third phase into our system.

2.3.2 Wetting & angle of contact

Surface properties are important when discussing the energetics of nucleation, specifically their role in determining the energetic barrier to nucleation since $W^* \propto \sigma^3$. If we consider a drop of water on a solid surface in a volume of air, we know that the water does not normally cover the solid as an extremely thin film, but has a distinct height and shape. This is a consequence of the same principle that drives nucleation, namely that the system wishes to minimize its potential energy. In this case, the drop does so by creating the most "cost-efficient" surface configuration. This means that an interface

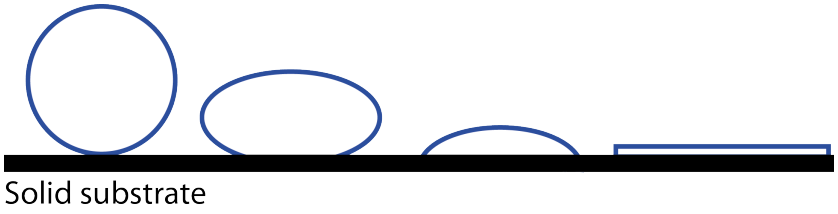

Figure 2.4: A figure demonstrating different angles of contact within the possible range. From left to right: $\theta_C = \pi$ (non-wetting), $\pi > \theta_C > \frac{\pi}{2}$ (partial wetting), $\frac{\pi}{2} > \theta_C > 0$ (partial wetting) and $\theta_C = 0$ (complete wetting). The last case is an infinetly thin liquid film covering the solid.

with more interactions across it, i.e. low interfacial energy, is preferred to one with fewer interactions, i.e. a high interfacial energy.

Figure 2.4 shows the effect of surface tension in a system where there is contact between three phases, namely a solid substrate, a gas and a liquid. In such systems it can be meaningful to define an equilibrium angle of contact, θ_C in Figure 2.5, which is the angle between the solid substrate and the gas-liquid interface where the three phases are in contact. Figure 2.4 demonstrates the range of possible angles of contact where we, from left to right, see an angle of contact of $\theta_C = \pi$, $\frac{\pi}{2} < \theta_C < \pi$, $0 < \theta_C < \frac{\pi}{2}$ and $\theta_C = 0$. The case where $\theta_C = 0$ really represent the case where the liquid covers the substrate as an infinitely thin film.

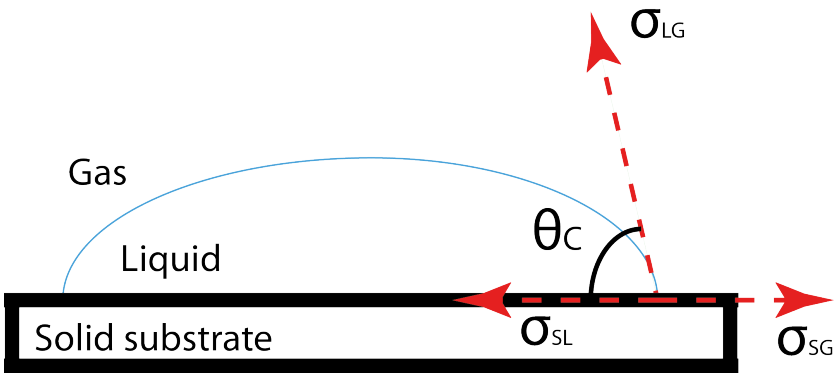

Figure 2.5: A figure showing the angle of contact defined in the point where all three phases are in contact.

This angle is derived from the considerations of Young by solving the surface forces at the point where the three faces are in contact, i.e. where the angle of contact is defined. One can define these force vectors from the surface

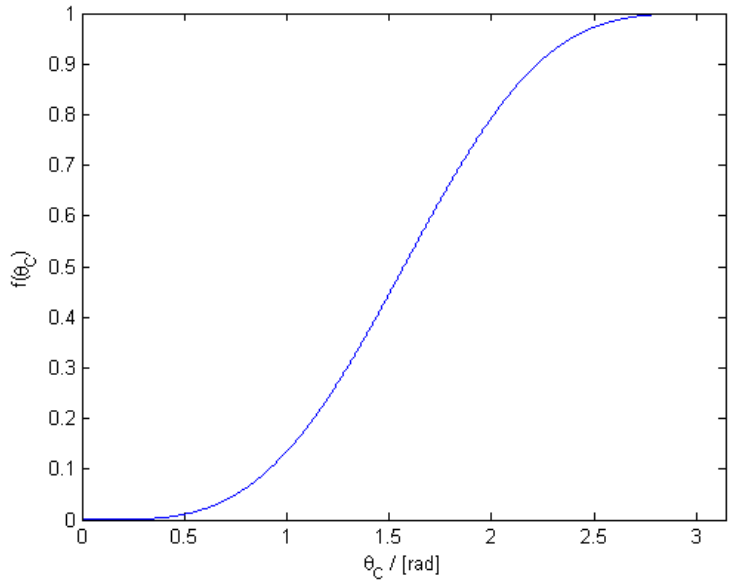

Figure 2.6: A plot of $f(\theta_C)$ for $0 \leq \theta_C \leq \pi$. The y-axis ranges from 0 to 1.

tensions is by considering them as being a force across a line per unit length, see the red arrows in Figure 2.5 [Feder, 1996]. Thus, one can sum up the horizontal forces, which at equilibrium must be zero, and be left with the expression

$$\sigma_{s,g} = \sigma_{s,l} + \sigma_{l,g}\cos(\theta_0) \tag{2.12}$$

After having defined the equilibrium angle of contact, one can define a function

$$f(\theta) = \frac{(2+\cos(\theta))(1-\cos(\theta))^2}{4} \tag{2.13}$$

which is plotted in Figure 2.6 [Kelton, 1991, Tiller, 1991, Mullin, 2001]. This function tells us how much the barrier to nucleation is lowered by introducing a third surface into a system by the equation

$$W^*_{3phase} = f(\theta)W^*_{2phase} \tag{2.14}$$

Consequently, if the equilibrium angle of contact is high (θ_C close to π), the barrier is not lowered much by introducing that surface into the system because $f(\theta_C)$ is close to one. Low angle of contact would, on the other hand, reduce the barrier considerably.

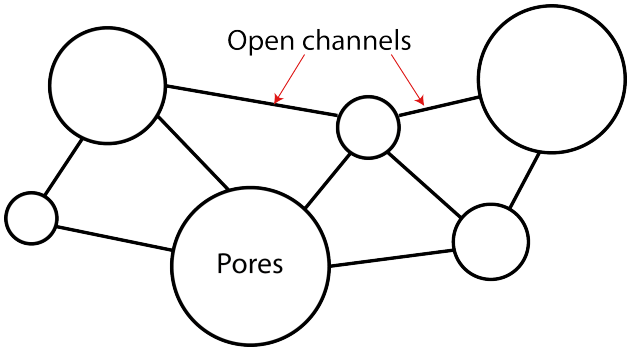

Figure 2.7: A schematic of how we typically define a porous media. The pores and channels are open to each other and they are surrounded by a solid matrix.

2.4 Nucleation in porous media

In this section we will apply some of the thermodynamics introduced so far to a porous media. The derivations are based on O. Vincent [2012] and Scherer [1993], and will describe cavitation and how crystals grow in confined volumes. In this section, porous media is defined as spherical pores connected by small channels, as shown in Figure 2.7.

2.4.1 Cavitation of liquids in confined spaces

Earlier we looked at the thermodynamics of a nucleating bubble or droplet, and we assumed that the surrounding volume was large enough to neglect any boundary or pressure effects during the nucleation process. If that is not the case, the volume of the surrounding material must be compressed or put under tension as the bubble grows given that the two phases have different molecular volumes. These derivations are taken from O. Vincent [2012].

Let us consider, for the sake of simplicity, a void bubble growing in a confined liquid. The compressibility of that liquid is given as

$$K_l = -V_l \left(\frac{\partial p_l}{\partial V_l} \right)_T \tag{2.15}$$

For small changes in pressure and volume, this can be approximated to

$$\Delta p_l = p_l - p_{l,0} = -K_l \frac{\Delta V_l}{V_{l,0}} \tag{2.16}$$

where the subscript 0 signifies the initial value before compression. The case of a void bubble is equivalent to a bubble consisting either of the vapor phase of the liquid or a gas that is soluble in the liquid. The only difference is a shift in the referance pressure [O. Vincent, 2012].

If we assume that the liquid is confined in a spherical volume of radius R_v, then the volume of the liquid is initially

$$V_{l,0} = \frac{4}{3}\pi R_v^3 \tag{2.17}$$

and the liquid volume in the presence of a spherical bubble of radius R is

$$V_l = \frac{4}{3}\pi R_v^3 - \frac{4}{3}\pi R^3 \tag{2.18}$$

The change in liquid volume is then given as

$$\Delta V_l = V_l - V_{l,0} = \frac{4}{3}\pi(R_v^3 - R^3) - \frac{4}{3}\pi R_v^3 = -\frac{4}{3}\pi R^3 \tag{2.19}$$

and inserting this in the equation for the change in pressure yields

$$p_l = p_{l,0} + K_l \left(\frac{R}{R_v}\right)^3 \tag{2.20}$$

The Laplace law for the liquid gives the equilibrium radius of the void bubble, R_{eq}, through $-p_l = \frac{2\sigma}{R_{eq}}$, so we can insert this into the previous equation to obtain

$$\frac{2\sigma}{R_{eq}} = -p_l = -\left(p_{l,0} + K_l \left(\frac{R_{eq}}{R_v}\right)^3\right) \tag{2.21}$$

If we then define a characteristic radius of the bubble on the form $R^* = -\frac{2\sigma}{p_{l,0}}$ similar to what we did in section 2.3, the equation boils down to

$$1 - \frac{R^*}{R_{eq}} = \gamma \left(\frac{R_{eq}}{R^*}\right)^3 \tag{2.22}$$

where

$$\gamma = \left(\frac{K_l}{-p_{l,0}}\right)\left(\frac{R^*}{R_{eq}}\right)^3 \tag{2.23}$$

is a parameter describing the confinement of the system. It can be shown [O. Vincent, 2012] that equation 2.22 only has a solution if $\gamma \leq \gamma_s = \frac{3^3}{4^4} \approx 0.1055$. Outside this region, no stable bubble can exist under tension and the

liquid is stable. γ can also be expressed in other ways. One way is through pressures as

$$\gamma = \frac{\Delta p_l(R^*)}{-p_{l,0}} \tag{2.24}$$

Qualitatively this helps us to explain the possible values of the confinement parameter. If the loss of tension at R^*, namely $\Delta p(R^*)$, becomes close to the intial tension, $p_{l,0}$, the expansion of the bubble would cause a positive pressure when $R \to R^*$. This positive pressure would collapse the bubble before it got over the nucleation barrier, i.e. before it could become stable.

γ can also be expressed through the systems physical parameters as

$$\gamma = \frac{8\sigma^3 K_l}{R_v^3 p_{l,0}^4} \tag{2.25}$$

where we see that changing the confinement parameter for a given system can be done by changing the radius of the confined space, R_v, i.e. the pore, or by changing the initial tension of the liquid, $p_{l,0}$.

This allows us to estimate the tension that water can sustain if we assume a confiment parameter.

$$-(p_{l,0})_c = \left(\frac{8\sigma^3 K_l}{R_v^3 \gamma_s}\right)^{\frac{1}{4}} \tag{2.26}$$

Figure 2.8 shows a plot of the maximum tension, $-(p_{l,0})_c$, at which liquid water is stable in pores of radius R_v. The choise of $\gamma = \gamma_s$ yields a lower bound estimate for the critical tension given a pore size, R_v.

2.4.2 Free energy for cavitation in a confined system

Now that we have seen how confinement allows systems to be stable at lower pressures it is time to study its energetics. O. Vincent [2012] derives the Helmholtz free energy of a system where confinement and compressibility is taken into account in the following way: If we assume small volume changes, the elastic energy that is stored in the compressed liquid per unit volume at constant temperature is given as

$$f_{el} = \frac{1}{V_l}\int_{p_1}^{p_2} p_l dV_l = \frac{p_2^2 - p_1^2}{2K_l} \tag{2.27}$$

In the last section we derived the liquid pressure as a function of initial pressure and compression due to a void bubble, i.e.

$$p_l = p_{l,0} + K_l\left(\frac{R}{R_v}\right)^3 \tag{2.28}$$

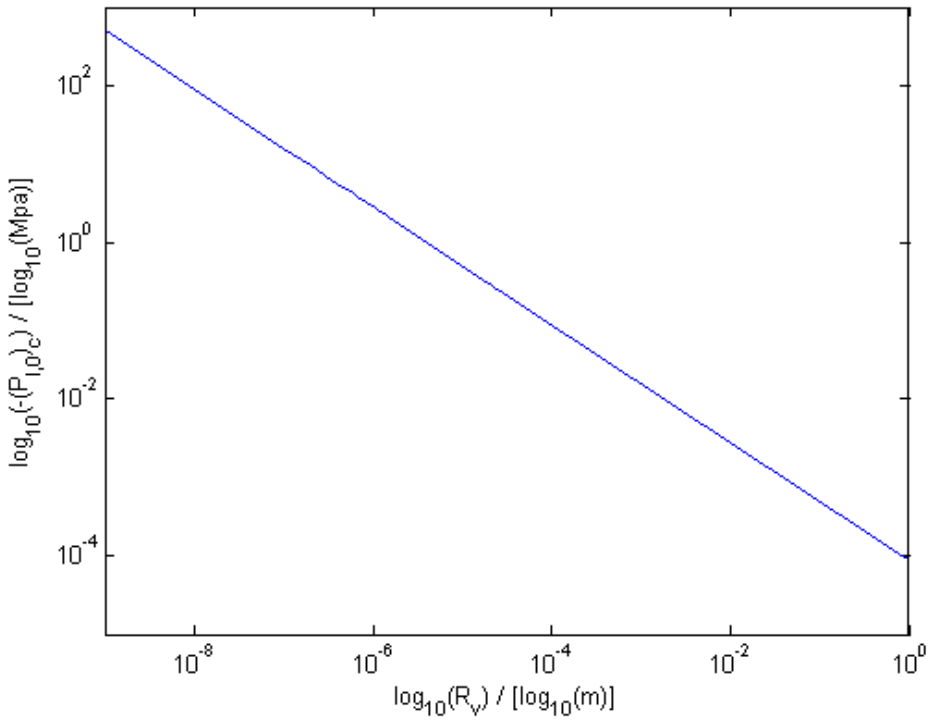

Figure 2.8: This figure shows a logarithmic plot of the region R_v between 10nm and 1m. These values are given at maximum confinement $\gamma = \gamma_s = \frac{3^3}{4^4}$ using the apropriate parameters for water at 20°C: $\sigma = 73 \times 10^{-3} \frac{N}{m}$ and $K_l = 2.18 \times 10^9$Pa.

If we let our system start with the negative pressure $p_1 = p_{l,0}$ and end up with a pressure $p_2 = p_l$ described by the above equation, we can find the total elastic energy of the system as

$$F_{el} = \frac{4}{3}\pi R^3 p_{l,0} \left(1 + \frac{K_l}{2p_{l,0}} \left(\frac{R}{R_v}\right)^3\right) \tag{2.29}$$

Using the definintion of γ found in the previous section and adding a surface term to the total free energy, namely $F_{sur} = 4\pi R^2 \sigma$, the cange in total free energy of the system with a bubble of size R, $\Delta F(R)$, can be rewritten on a dimensionless form as

$$\frac{\Delta F(R)}{\Delta F^*} = -2\left(\frac{R}{R^*}\right)^3 \left(1 - \frac{\gamma}{2}\left(\frac{R}{R^*}\right)^3\right) + 3\left(\frac{R}{R^*}\right)^2 \tag{2.30}$$

We recognize that compared to a non-confined system, equation 2.11, the confinement has altered the term that was proportional to R^3. Now, we have one term proportional to R^6 and one proportional to R^2. This gives the system an additional minimum on the free energy curve for $R \neq 0$ corresponding to the solution of equation 2.22. We also note that when $\gamma = 0$, the equation reduces to equation 2.11 which is plotted in figure 2.3.

As we already know, equation 2.22 has no solution for $\gamma > \gamma_s$, so for these confinement parameters, the free energy has no minimum for $R \neq 0$. However, for $\gamma < \gamma_s$, the curve displays a minimum for $R > R^*$ as shown in figure 2.9(a). We also note that for the range of confinement parameters between γ_s and γ_t, the minimum has a higher value than at $R = 0$. This means that the new minimum created by the confinement is a metastable state. For $\gamma < \gamma_t$, the minimum is lower than the state without a bubble, $R = 0$, and the minimum represents the equilibrium energystate, figure 2.9(b). The transition confinement parameter is found to be $\gamma_t = \frac{1}{16} \approx 0.0625$ [O. Vincent, 2012].

2.4.3 Melting point

Let us now consider the melting temperature of a small crystallite. We know from the Young-Laplace equation, equation 2.5, that the pressure of a small crystal is a function of the pressure of the surrounding liquid, the surface energy and the curvature. To derive equation 2.5, we assumed we had a spherical cluster, for an ellipsoid, the curvature is given as

$$\kappa_{CL} = \frac{1}{r_1} + \frac{1}{r_2} \tag{2.31}$$

where the subscript indicates that it is the curvature of the crystal-liquid interface and r_1 and r_2 are the two principal radii of curvature of the cluster. This allows us to rewrite equation 2.5 to

$$P_C = P_L + \sigma_{CL}\kappa_{CL} \tag{2.32}$$

Note that for a spherical cluster this reduces to equation 2.5 because $r_1 = r_2 = R$. The Gibbs-Duhem equation is given by

$$SdT - VdP + Nd\mu = 0 \tag{2.33}$$

If we divide both sides with N we end up with molar quantities (or units of N). If we do this for both the liquid and crystal we get

$$d\mu_L = -S_L dT + v_L dP_L \tag{2.34a}$$

$$d\mu_C = -S_C dT + v_C dP_C \tag{2.34b}$$

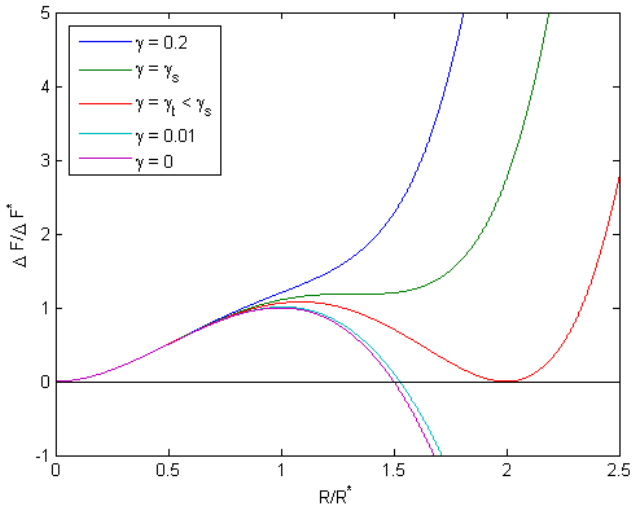

(a) Free energy for several γ.

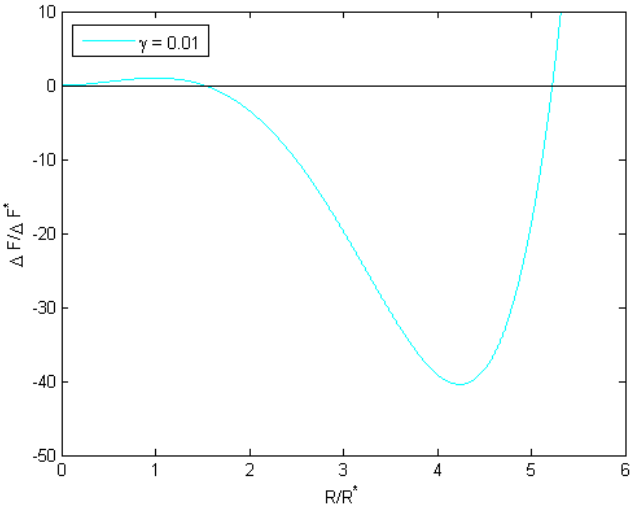

(b) Free energy minimum for $\gamma = 0.01$.

Figure 2.9: A dimensionless plot of the free energy of a confined system as a function of void bubble radius. The plot shows the energies for a selection of confinement parameters. Note the different scales on the plots.

where S is the molar entropy and v is the molar volume.

We know that in equilibrium, $d\mu_C = d\mu_L$, so equating both right hand sides of equation 2.34, and taking the total differential of equation 2.32, i.e. $dP_C =$

$dP_L + d(\sigma_{CL}\kappa_{CL})$, we get

$$\frac{S_L - S_C}{v_C} dT = \Delta S_{fv} dT = \frac{v_L - v_C}{v_C} dP_L - d(\sigma_{CL}\kappa_{CL}) \tag{2.35}$$

where $\Delta S_{fv} = \frac{S_L - S_C}{v_C}$ is the entropy of fusion per unit volume of crystal.

The normal melting temperature at the triple point is T_m, which corresponds to a large flat crystal ($\kappa_{CL} = 0$) in contact with a liquid that has a pressure equal to its vapor pressure, P_e. Using this as initial conditions, we can integrate the above expression [Scherer, 1993]

$$\int_{T_m}^{\tilde{T}_m} \Delta S_{fv} dT = \int_{P_e}^{P_L} \frac{v_L - v_C}{v_C} dP_L - \int_0^{\sigma_{CL}\kappa_{CL}} d(\sigma_{CL}\kappa_{CL}) \tag{2.36}$$

Here, $\tilde{T}_m$ is the melting temperature that has been displaced from T_m due to the curvature and applied liquid pressure, P_L. If this effect is not too large, the above expression can be approximated to

$$\tilde{T}_m - T_m \approx \left(\frac{v_L - v_C}{v_C} \right) \frac{P_L - P_e}{\Delta S_{fv}} - \frac{\sigma_{CL}\kappa_{CL}}{\Delta S_{fv}} \tag{2.37}$$

As an example, if we have a crystallite in a liquid, which in turn has a planar interface with a gas, then $P_L = P_e$, and equation 2.37 reduces to the Gibbs-Thompson equation

$$\tilde{T}_m \approx T_m - \frac{\sigma_{CL}\kappa_{CL}}{\Delta S_{fv}} \tag{2.38}$$

Since ΔS_{fv} is positive for almost all substances, and we already know from equation 2.5 that $\sigma_{CL}\kappa_{CL}$ must be positive, a small crystallite has a lower melting point that a large or flat crystal.

Another example is the Clapeyron effect. If we start with equation 2.37, and instead assume that the curvature is negligable, we obtain

$$\tilde{T}_m = T_m + \left(\frac{v_L - v_C}{v_C} \right) \frac{P_L - P_e}{\Delta S_{fv}} \tag{2.39}$$

When a substance undergoes a phase change in a finite volume, we know that due to the difference in molecular volume, there will be a pressure change. This pressure change will result in a shift in the phase diagram, effectively changing the melting temperature, $\tilde{T}_m$. This is what equation 2.39 tells us given that we have a system large enough for the effect of curvature to be ignored.

For water, this has a special effect. We know that for most substances, the solid phase has a lower molecular volume than the liquid phase. Ice, on the other hand, has a higher molecular volume than water. This leads to a lower melting point with increased compression, P_L. In other words, if a volume of water is incased in an ice crust, the crust will try to oppose the expansion of the water inside. This sets up a pressure on the water which reduces its melting point.

Now that we know the effect of both curvature and confined volume on the melting point, and the fact that we have a barrier to nucleation, we know that for an ice crystal to grow in a pore we must first overcome the barrier to produce a nucleus. In a pore network, like the one shown in Figure 2.7, the barrier will most likely be somewhat lowered by the matrix which makes up the pore wall, and the nucleation will be heterogeneous. Once we have a stable nucleus, it will grow until it fills the pore. While it is sufficiently small, however, it will be subject to the pressure set up by the curvature (Gibbs-Thompson effect). When it becomes bigger, it will be affected by the pressure set up by the pore walls due to the volume change when the water freezes to ice (The Clapeyron effect). Both of these effects demand that for the crystal to grow, $T \leq \tilde{T}_m$ for the appropriate conditions. The assumption behind this specific scenario is that it is energetically preferable to grow a crystal in the pore as opposed to growth on the walls of the channels connecting the pores. Specifically that the matrix has either a sufficiently high equilibrium angle of contact, θ_C, or that the channels are small enough such that a growing crystal would need to adopt a curvature that is too high or both. Let us assume that this assumption applies.

Given that we now have a pore completely filled with ice, the only place it can continue to grow is in the channels. For the ice to start growing, it must adopt the shape of the channel, giving it a distinct criterion for the curvature. Scherer [1993] gives this criterion for a cylindrical pore of radius r as

$$\kappa_{CL} = \frac{-2\cos(\theta_C)}{r} \tag{2.40}$$

Essentially, the temperature must be lower than $\tilde{T}_m = \tilde{T}_m(P_L, \kappa_{CL})$ for the crystal to grow given the needed curvature.

In this chapter, the thermodynamic theory of nucleation has been considered for both infinite and finite systems. With this in mind, he following chapter will describe the development of an experimental method for studying nucleation in porous media.

Chapter 3

Development of the experimental method

3.1 The experimental idea

The object of this thesis has been to study nucleation and cavitation using an experimental setup that allows for in situ observations. More specifically, we wished to study:

- Freeze-thaw cycling and the subsequent formation of gas bubbles from dissolved gas at positive pressures with a constant volume of water and gas.
- Freeze-thaw cycling and cavitation, which requires negative pressures created by evaporation of water.
- The effect of connected pores in a network subject to freeze-thaw cycles as opposed to isolated pores.

To realize these goals, we needed to control three aspects, namely the sample, the enviroment that the sample was subject to and the measurements.

3.2 The setup

To create a setup which allows for direct inspection of the nucleation and growth processes, a simple setup was used, see figure 3.1. A camera (ProSilica GC1350) and a light source were placed on either side of a sample containing

the water filled porous material. The camera, light source and sample holder were mounted on an aluminum plate. Detailed descriptions of the samples used will be presented in section 3.3. The freezing of the system was done by placing the setup in a sealed box which was put in a freezer that held an approximate average temperature of $-28°$C.

The samples were initially illuminated by a single LED light source (LT PR 36, Opto Engineering), but for the majority of experiments conducted, a circular LED light was used. The circular LED was made by connecting 32 small LEDs (Elfa, L5-G61N-GT) together forming a 7cm diameter ring and mounting them on a veroboard. When using a single LED light source it was set at an angle such that only light reflected from an interface would be directed into the lens. This is shown in figure 3.1(a). When the ring LED was used the center was placed directly behind the sample such that the incident light would hit the sample uniformly from all sides yet still at an angle, see figure 3.1(b). The ring LED lighting technique was used in order to secure uniform light conditions while maintaining an increased contrast between ice and water.

The plastic box that the setup was placed in was sealed with a lid. To avoid condensation on the equipment or on the sample surface, a dehumidifier (Chameleon, silica gel C 1-3mm) was placed under the aluminum plate that the setup was mounted on, see figure 3.1(b). The temperature was measured by a thermistor (NTC-resistor, Elfs RH16-4A104GB, 100kΩ) mounted on the sample and connected to a NI-DAQ USB-6211. The thermistor was mostly mounted close to the block of PDMS on the sample using electrical tape and a thermal paste (Wacker Wärmleitpaste P12) to ensure good thermal contact. The camera, lightsource and temperature measurements were controlled by a computer running LabView v10.00. When a camera with a higher framerate was needed, the ProSilica GC1350 was substituted with an Edmund Optics EO-0413C controlled by a secondary computer running uEye software. This led to an average framerate of 82fps.

Thermistor calibration was performed using a quartz probe thermometer (HP 2804 A). The voltage drop measured over the thermistor was then fittet to the temperature measurement using the function given by the manufacturer.

$$\frac{1}{T} = B \ln\left(\frac{V}{V_0 - V}\right) - C \tag{3.1}$$

In the equation, V_0 is the total voltage over the circuit (100kΩ coupled in series with the thermistor) and V is the drop over the thermistor. A linear fit

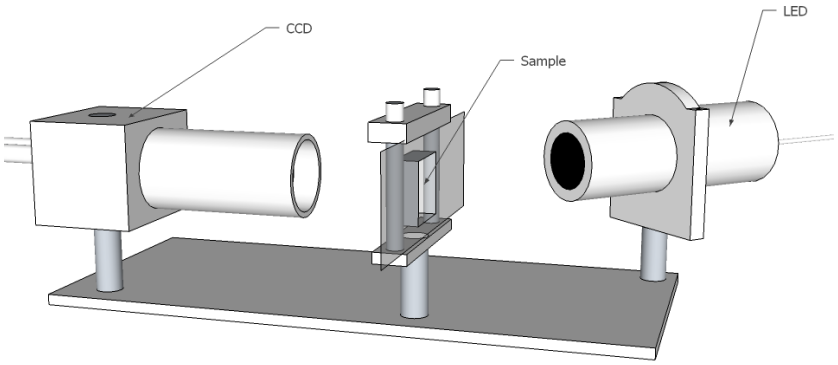

(a) A schematic of the experimental setup used in some of the experiments.

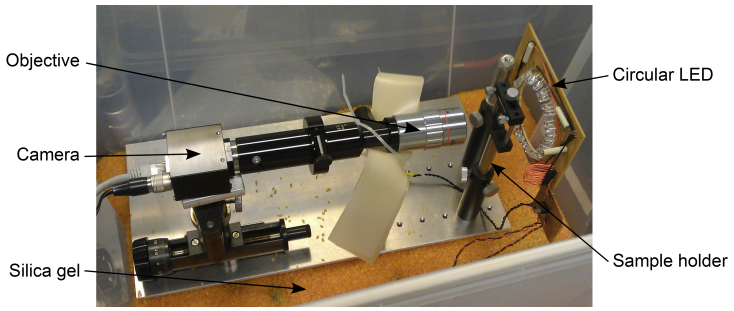

(b) A picture of the set up with the ring LED light source on the right and the camera equipped with a microscope lens.

Figure 3.1: The experimental setup used in the experiments.

of $\frac{1}{T}$ on $\ln\left(\frac{V}{V_0-V}\right)$ gave the parameters $B = 3653.8$ and $C = 12.185$. These will be used throughout the thesis.

Using these parameters, the standard deviation of the estimated temperature from the thermistor measurements minus the temperature measured by the quartz probe thermometer was $\Delta T_q = 0.115$K and the manufacturer sets an error between individual thermistors which yields an additional $\Delta T_t = \pm 0.4$°C. For the remainding of this thesis, an error of $\Delta T = \pm\sqrt{\Delta T_q^2 + \Delta T_t^2} = \pm 0.42$°C was used. Note that it is assumed that the error in the measurements of the quartz probe thermometer is negligible compared to ΔT.

The lenses and cameras used in this thesis were calibrated, and the corresponding resolutions are listed in table 3.1. Three lenses were used, two microscope lenses (2X Mitutoyo Plan Apo Infinity-Corrected Long WD Objective & 5X Mitutoyo Plan Apo Infinity-Corrected Long WD Objective)

and one photolens (Computar, MLM3X-MP 0.3-1.0X) wich was used with either maximum or minimum zoom (1.0X or 0.3X respectively). Because the resolution of the microscope lenses used were higher (or equal to) the pixel resolution of the cameras, the pixel resolution has been used as a measure of the resolution of the pictures taken with these lenses. As the photolens was used to study large scale effects, only the pixel resolution is presented in table 3.1.

Camera	Lens	Resolution in μm/pix
ProSilica:	photolens (no zoom)	12.5
-	photolens (max zoom)	5
-	$\times 2$	2.5
-	$\times 5$	1
Edmund Optics:	photolens (no zoom)	25
-	photolens (max zoom)	10
-	$\times 2$	5
-	$\times 5$	2

Table 3.1: A table of the resolutions used in this thesis for the two cameras with the three lenses.

3.3 The samples

To reach the goals, two different types of samples were used. The first type was made for studying nucleation in a network of pores of varying size, comparable to the tracheid network in the xylem of natural trees. The material used was a type of silicone rubber called polydimethylsiloxane (PDMS). The second sample type was made from hydrogel. This material is known for its diffusive properties, and it was the material of choice for Wheeler and Stroock [2008]. The pores in the hydrogel were isolated and of uniform size. These samples were used to study nucleation in isolated pores. The difference in behavior between the two sample types was used to illustrate the difference between nucleation in isolated and connected pores.

The following section will describe the trial and error in developing a PDMS sample which could be used in the proposed setup. The obstacles will be explained in further detail, but the main issue was retaining a constant volume of water and gas in the PDMS samples. The preparation and treatment of the hydrogel sample will be discussed before presenting the results of the experiments.

3.3.1 PDMS sample structure & preparation

To test this setup, experiments were performed using capillary tubes glued onto a glass slide as samples, see table 3.2. The glue used was a UV curing glass glue (Casco Glaslim).

Exp name	Sample	Preparation	Notes
*120119	CAP01	Two partially filled (about 90%) and sealed glass capillary tubes of size $0.2 \times 4.0 \times 100$mm mounted on a glass slide with a UV-curing glass glue.	The bottom one broke and was drained prior to freezing.
*120519	CAP02	Three partially filled (over 95%) capillary tubes of unform length (50mm) with cross sections 0.2×4.0mm, 0.1×1.0mm and 0.05×0.5mm mounted as above.	All three burst on freezing.

Table 3.2: Table describing the experiments conducted on capillary tubes. The *-notation in the experiment name column indicates that the results will be presented in chapter 4. This notation will be used throughout the remaining chapter.

To gain insight into what happens in tracheids in the xylem of trees we created a network of pores connected by small channels, where the pores represent a thin crossection of tracheids. The channels connecting the pores act as pit openings that connect tracheids. They are also needed to be able to fill the network with water by injection with syringes. The details on the filling procedures used will be explained later in this section.

The pattern used was made by creating a postscript file using MATLAB, an example is shown in Figure 3.2(a). We chose the pore radii to be between 20 and 500μm, and the total number of pores were 100, 300, 1000 and 3000. The desired number of pores were placed at random while ensuring that no pores overlapped. The pore radii were chosen at random within the desired interval. For the mold with 3000 pores, the pores were stacked so closely that the casts that were made did have some overlapping pores. After the pores had been placed, nearest-neighbour pores were connected with channels using Delaunay triangulation. This process insured pore networks without any intersecting channels.

The technique used to create the molds was soft photolithography. The process involves taking a thin silicon wafer covered with a UV-curing resin and placing the desired pattern in contact with the resin before subjecting it to UV light. The parts of the resin surface that is not hit by light is washed away leaving a raised pattern on the surface of the disc. Two sets of the

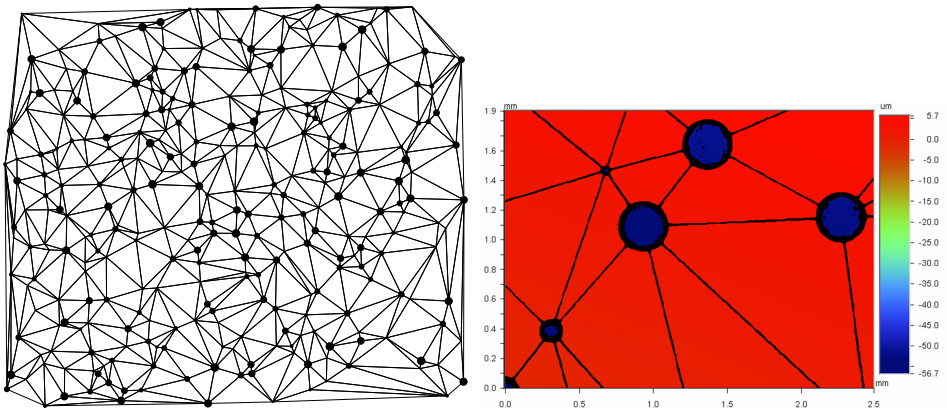

(a) One of the networks generated by the MATLAB script.

(b) An interferometry image taken of a block of PDMS.

Figure 3.2: The images show the MATLAB generated postscript image of the network used to make the molds ((a)) and an interferometric image of one of the resulting casts made with PDMS ((b)). The size of the entire network is approximately 19×22mm. Note that the black area on the interferometry image was not possible to measure due to the steepness of the pore wall.

same molds were ordered from Laboratoire Interdisciplinaire de Physique at the Université de Grenoble, one with a height of 50μm and one with 200μm. Only the molds with a height of 50μm were used in the experiments and a cast made from one of the molds is shown in an interferometer image in figure 3.2(b). Some of the molds ordered are shown in figure 3.3. These molds were used to create casts of the desired patterns as will be described in the following paragraph.

The medium used to create the cast of the mold was a polydimethylsiloxane (PDMS) which is a type of silicone rubber. PDMS has the advantage of being easy to make and it can adhere to glass without using any form of glue or other adhesive. Initially we thought of PDMS as a water-tight soft material that would allow the volumes of water and gas in the network to remain constant while being able to sustain the volume changes associated with freezing. This is not the case, and the following sections will describe the methods used to compensate for this.

To make the PDMS casts, the procedure was to first mix the monomer (Sylgard 184 silicone elastomer) and add 10% curing agent (Sylgard 184 silicone elastomer curing agent). This, still liquid PDMS, was put into a desiccator connected to a vacuum pump (Ilmvac MPC 101 Zp) to get rid of small bubbles that might reduce the optical qualities of the PDMS when it hardened.

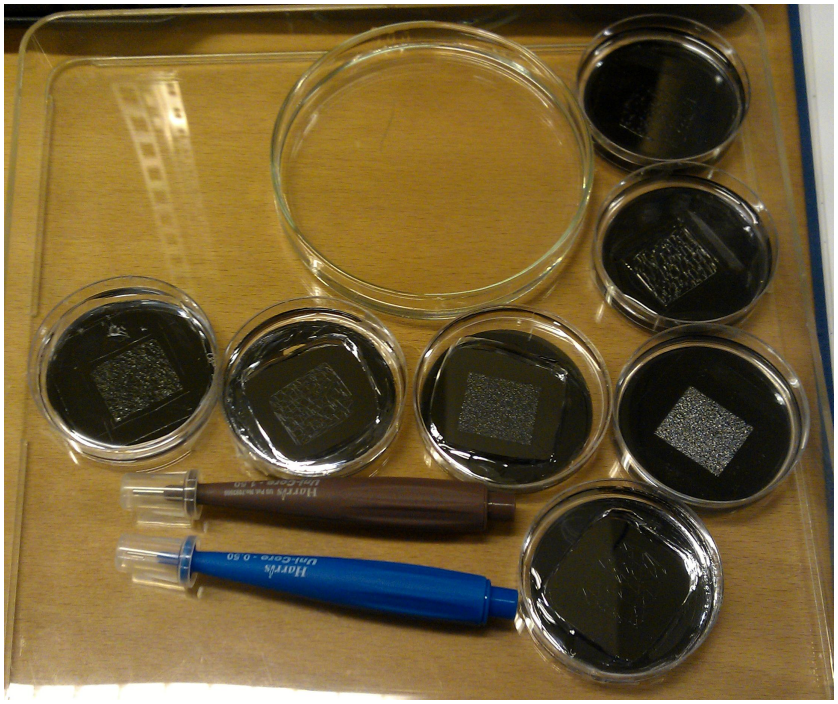

Figure 3.3: A picture of some of the molds used for the experiments. The blue and brown knives used to cut cylindrical holes are shown (bottom left). The circular containers are approximately 5cm in diameter.

After removing the bubbles, the PDMS was poured over the mold and set to harden in an oven at 60°C for an hour. After hardening, the PDMS was cut from the mold and two small cylindrical holes were cut vertically through the PDMS in opposite corners to allow for injection of water. The knives used to cut the molds are shown in figure 3.3. To adhere the PDMS to glass, both surfaces were cleaned and treated with plasma using a high frequency generator (ETC, BD-20 ACV) connected to an electrode before mounting the PDMS onto the glass. The soft PDMS takes on the shape of the glass well, but in addition, this treatment ensures that the PDMS surface is clean and the plasma removes all absorbed atoms from the surface allowing it to adhere better. Finally, sample was put back in the oven to cure for another 2-3 hours at 60°C. A typical result is shown in figure 3.4.

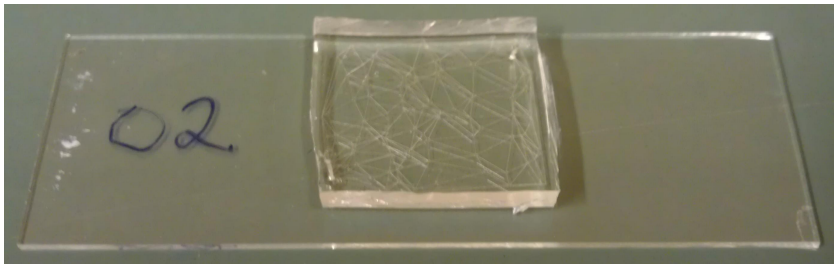

Figure 3.4: A picture of the basic sample used (sample PDMS02). Injection points are in two opposing corners namely lower left and upper right. The glass slide on which the PDMS is mounted has dimensions 25×75mm (1mm thick).

3.3.2 Plugging the holes

Initially, the samples were filled using syringes and the injection sites were left open while taking pictures. After a while we saw effects that indicated that the water in the samples dried up (table 3.3, experiment name 120206). To test if the drying was due to intrusion of air through the open injection sites, different methods of sealing the holes were attempted. Four tests were performed (table 3.3) where the substances used were:

- vaseline
- silicone grease (Wacker), typically used for lubricating desiccators
- silicone based glue (Wacker Elastosil A07)
- fast curing epoxy (Biltema, Quick-epoxy)

In addition, the syringes were left while still connected to the sample during the experiment (table 3.3). The preparation of each sample took approximately four hours, and drying was observed either after a few hours or when the sample was left over night. All samples were either close to or completely dry over night, and the observations led us to conclude that the samples were not stable for more than a few hours. Because we had one set of molds, creating equal samples required that only one cast could be made every two hours.

The observations made indicated that all samples dried in a similar manner. The areas that dried first were the areas close to the injection sites. This was observed through a microscope (Olympus, SZX2-ILLT), and the distinction between gas and water in the pore network was based on the observation of

menisci formed between the water filled and gas filled part of the network. These menisci were easily observed using the microscope.

The fact that the areas around the injections sites dried first indicated that it could not be evaporation at the injection sites that was the problem. Nor could it be leaking from the injection sites as no water was present there shortly after the onset of drying. Instead, it suggested that water was diffusing out through the PDMS matrix. This would also explain why the drying appeared to begin at the injection sites. When the injection sites were left open, the volume of water that had diffused out had to be replaced by gas which was pulled in through the injection sites. When the sites were sealed, it is likely that some small volume of gas was present under the seal. When diffusion had set up a sufficiently low pressure, this volume of gas would expand, resulting in effects indistinguishable from the ones observed when the injection sites were left open. Furthermore, it is possible that some of the attempted seals were not air tight, allowing some seepage of gas when the pressure became sufficiantly low. We concluded that the PDMS was not diffusion proof and thus not as water tight as we initially believed it to be.

Exp name	**Sample**	**Preparation**	**Notes**
120206	PDMS01	Basic sample (figure 3.4): PDMS with injection holes mounted on a glass slide.	No apparent freezing down to -22°C. Confirmed that it was dry with a microscope after the experiment.
*120208	PDMS01	Tubes connecting syringes and injection holes were cut close to the PDMS and sealed with fast curing epoxy.	Sample was only partially filled, observed freezing at -13.3°C.
120220	PDMS01	Sealed with epoxy.	No observable freezing at -20°C.
120221	PDMS03	Sealed with epoxy.	Confirmed that sample was $\approx$ 100% full. Dried during one night.
*120222a	PDMS03	Sealed with epoxy.	Observed onset of drying in a matter of minutes.
*120222b	PDMS03	Refilled sample, but instead of sealing, the Luer-lock valves on the syringes were shut left in during the experiment.	Drying started after 2h16m.
120227	PDMS01	Sample filled with tap water and sealed at injection sites with Wacker Elastosil A07	No significant effect.
*120516c	PDMS02	Injected water, no seal.	Drying started after 90 seconds.
*120523b	PDMS17	Luer-lock valves shut and left in.	Used a higher speed camera (about 82fps) to observe two stage freezing with a higher time resolution.

Table 3.3: List of the first experiment with PDMS and the subsequent experiments conducted to seal the injection sites. The experiment did not include freeze-thaw cycles unless stated under "Notes".

3.3.3 Dealing with diffusion

Watson and Baron [1996] reported that water has a diffusion coefficient of about $2 \times 10^{-9} \frac{m^2}{s}$. This is close to typical diffusion coefficient of solutes in water [Robert C. Weast, 1984] and it is far too high to be able to consider the volume of water as constant in the timespan of the freeze-thaw part of the experiments, which is typically 4-6 hours.

If we assume a simple diffusion model with a constant diffusion coefficient equal to that of PDMS ($D = 2 \times 10^{-9} \frac{m^2}{s}$) and initial conditions $C = C_0 (0 < x < 50 \mu m)$ at time zero, we have a one dimensional system that is similar to the PDMS. Crank [1979] offers the solution to the equation on the form

$$C(x) = \frac{1}{2} C_0 \left(erf \frac{h - x}{2\sqrt{Dt}} + erf \frac{h + x}{2\sqrt{Dt}} \right) \tag{3.2}$$

where h is the width of the initial distribution (50μm). Inserting values corresponding to those of PDMS, the consentration distribution can be plotted through time (figure 3.5). From the figure we see that the diffusion coefficient is so high that the systems water is depleted in a matter of seconds, which is not far from experiment 120516c (table 3.3) where the injection sites were left open and the sample started drying after 90 seconds. The mismatch between this system and the other experiments is that when the injection sites were covered, the system struggles to replace the volumes of water that diffuses out and a lowered pressure is generated which reduces the rate of diffusion. This simple model was included to demonstrate the diffusive abilities of the PDMS material, but it does not compare well to the general behavior of the samples when the PDMS treated as described in this and later sections.

This explains why sealing the injection sites would not suffice, which was indeed what our observations led us to believe. In order to slow down this process, some form of non-diffusive barrier on the surface of the PDMS might prove effective. As glass can be considered diffusion proof, at least over the times involved in the experiments, an idea to hinder diffusion at the surface was to cover the surface with a secondary glass slide and to connect the remaining sides of the PDMS to a reservoir of water.

The preparation was done by first mounting the PDMS onto a glass slide like before (figure 3.4). The sample was filled under water using syringes and left to soak in a bath at room temperature. After 30 minutes, it was examined for bubbles and refilled if needed. Then, the sample was left overnight to soak in a bath in order to assess whether the PDMS would saturate if left in water. The next day, the surfaces of the sample were dried before placing sanitary

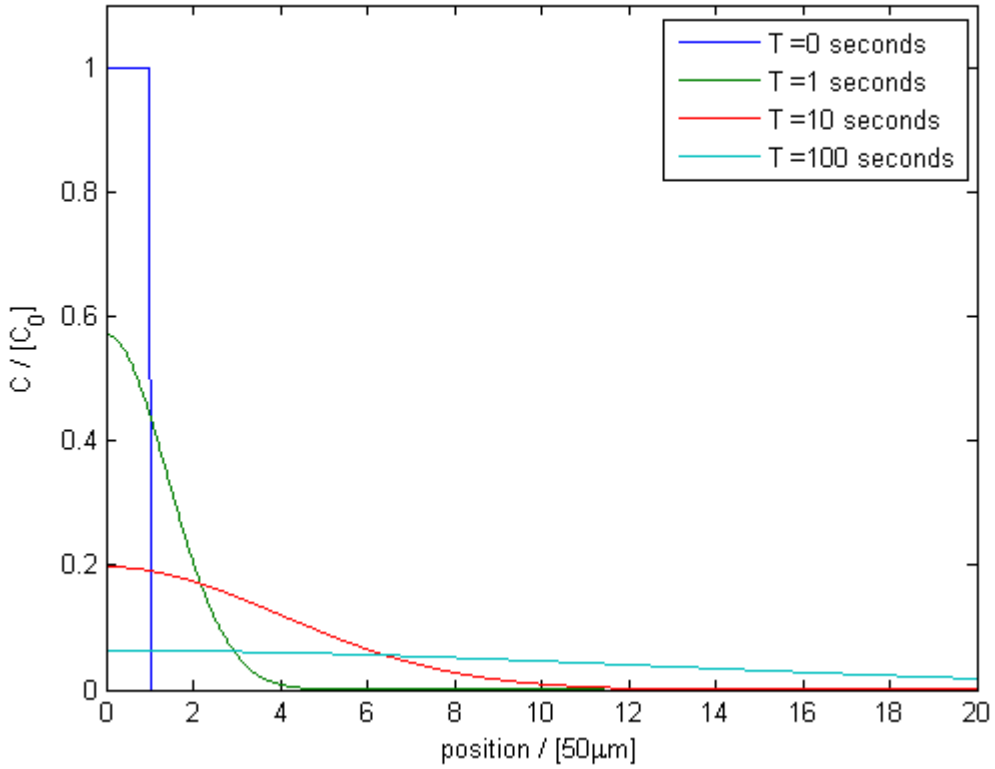

Figure 3.5: A plot of the concentration distribution in a simple diffusion system modelled after PDMS with 50μm high pores. Time = 0 seconds shows the initial distribution.

silicone (Casco) on the glass slide to include reservoirs. Subsequently, a second glass slide was glued on top of the PDMS slab using the UV-curing glass glue. A picture of the sample is shown in 3.6. Some additional experiments on soaking were conducted. These are included in table 3.4.

This preparation slowed the diffusion process significantly, and the optical quality was not degraded from the UV-curing glass glue or the glass covering either side of the PDMS. The only drawback was that the silicone needed approximately 24 hours to cure, and by that time the system had already started to dry. A list of the experiments conducted can be found in table 3.4.

Other attempts were made to circumvent diffusion. They were based on simply trying to coat the surface of the PDMS with a diffusion proof substance. A silicone grease was tested and a sample made using this technique is shown in figure 3.7(a). The silicone grease reduced the transparency, making the

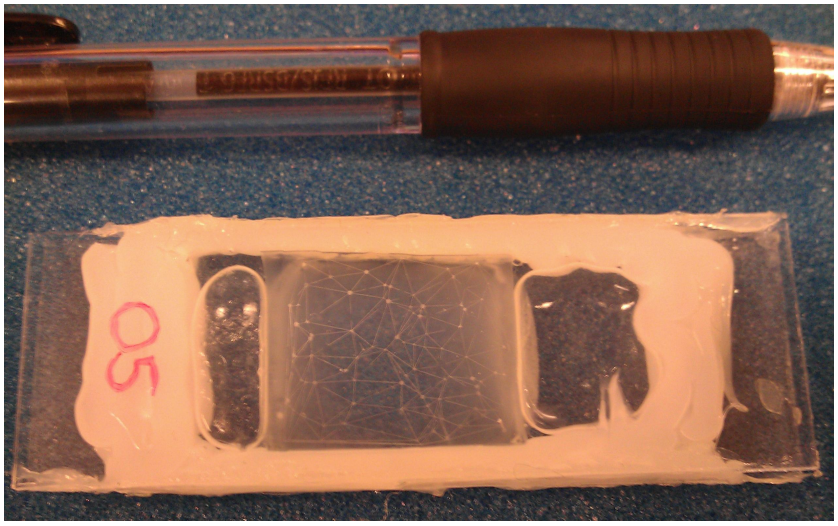

Figure 3.6: A picture of one of the samples where sanitary silicone and an additional glass plate was used. The bubbles in the reservoirs were not present initially and is most likely the result of diffusion from the PDMS, diffusion from outside the sample or both. The glass slides are 75×25mm and they are 1mm thick.

optical quality of the sample quite poor, and it did not improve the time in which the volume of water was allowed to remain constant. In addition, the grease was not viscous enough to ensure that it would continue to cover the corners of the sample for the duration of one experiment.

(a) A sample covered with silicone grease. (b) A sample covered with a UV-curing glass glue.

Figure 3.7: Examples of surface treated samples made to prevent diffusion of water out of the system. The sample shown in (a) is sample PDMS06 and the one shown in (b) is PDMS07 (table 3.4). The glass slides are 75×25mm and they are 1mm thick.

To improve on the transparency and viscosity, and to test whether the silicone grease was merely a poor choice in material, a UV-curing glass glue was also used to cover the open surfaces of the PDMS. It slightly improved the optical quality (figure 3.7(b)), but the diffusion was not sufficiently slowed down.

The failing in keeping the volume of the water constant might be explained by diffusion into the interpolymer spaces in the PDMS, given that PDMS does not saturate in a bath at room temperature.

Exp name	Sample	Preparation
*120224	PDMS03	Sample filled and treated with sanitary silicone and a second glass slide. Reservoirs included and filled. Cured for 12h.
120305	PDMS05	Same as above, but left in a bath at room temperature overnight before being treated with silicone.
120307	PDMS04	Sample mounted on large quadratic glass plate. Bath at room temperature for over 72 hours. Refilling when needed. Covered with vacuum grease.
120308a	PDMS06	PDMS mounted on glass with injection sites. Filled and left in a bath at room temperature for over 24 hours with contiued refilling when needed.
120308b	PDMS06	Sample saturated for 6 days. Sealed surfaces with vacuum grease.
120308c	PDMS07	Resaturated and refilled.
120308d	PDMS07	Resaturated and refiled. Dried the surface quickly and covered surface with UV-curing glass glue.

Table 3.4: A table describing the various experiments conducted trying to seal the samples to avoid the effects of diffusion. All of the samples started drying within 12 hours.

3.3.4 Saturating & sealing

The results from the treatment described in the previous section were most likely due to that the PDMS was not saturated, but [Randall and Doyle, 2005] has shown that PDMS can be saturated if soaked in water at a temperature of 50°C for a period of approximately 24 hours. With this in mind, the method of covering the sample with a non- or slowly diffusive barrier could still be viable. Since the silicone, glass and reservoir method gave the best optical qualities compared to covering the entire surface with a material, a new method was developed along those lines with a focus on avoiding the long curing period of the silicone.

This method was, after mounting the PDMS onto the first glass plate, to fill it and put the sample into a closed container and let it soak at 50°C for 24 hours. Then, the sample was taken out of the container, the surfaces were dried quickly using tissue paper and a second thin cover glass, slightly larger than the PDMS surface, was attached using a UV-curing glue. The sides were then covered with a fast curing epoxy (figure 3.8(a); for a schematic cross section, see figure 3.8(b)). This approach led to a significant decrease in sample preparation time compared to the treatment with the sanitary silicone, and the time before the pores started drying was comparable. Consequently,

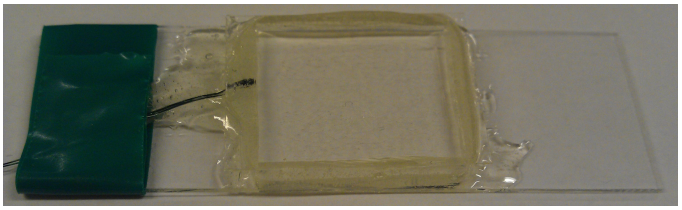

(a) A sample where a thin cover glass has been glued on the top and epoxy covers the sides. The thermistor is also visible on the left side of the sample.

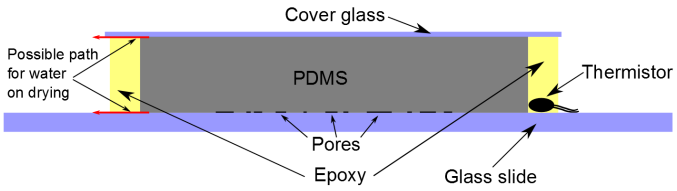

(b) A schematic cross section of the samples that were prepared with a cover glass and epoxy.

Figure 3.8: Figure (a) shows the sample with the thermistor placed as described in the text. The glass slide is 75×25mm. Figure (b) shows an illustration of a cross section of the sample (not to scale). In reality, the height of the pores is approximately 1/100 of the thickness of the PDMS.

it became the method of choice when studying systems during freeze-thaw cycles. As a bonus, this method allowed for the thermistor to be placed inside the layer of epoxy and thus be in good thermal contact with the part of the sample that acts as a thermodynamic reservoir for the sample system (figure 3.8(a)). The experiments conducted with this method are listed in table 3.5.

Exp name	Sample	Preparation	Notes
*120315	PDMS08	Sample saturated at 50°C for 48 hours. Sealed with cover glass and epoxy.	Conducted freezing experiment over four cycles to try to observe the growth of stable bubbles over consecutive cycles. Non were observed
*120320	PDMS09	Same as above.	Same as above, but ice was already present during freezing on the second cycle. The experiment was stopped after that such that only one cycle was completed.
*120322	PDMS 10	Same as above with the addition of waterfilled cylindrical reservoirs cut into the PDMS on the short ends.	Observed two stage freezing.
*120330a	PDMS12	same as above	Took pictures of two stage freezing with a microscope lens.
120330b	PDMS12	continued from previous	Tried to observe drying over a period of five days. No drying observed in that field of view. Manual inspection revealed about 50% of the pores had dried.
*120404	PDMS12	continued from previous	Changed the field of view to find a meniscus that could be observed. It did not move for 24 hours. (Sample did dry after about a week.)
*120405	PDMS11	Sample filled and saturated before glass and epoxy	An experiment that only focused on observing drying.
*120607	PDMS18	Hot bath ¿ 12h, glass and epoxy.	Used a camera with higher time resolution to and a microscope lens to capture two-stage freezing and thawing.

Table 3.5: A table of the experiments conducted using the saturation procedure and the glass, UV-curing glass glue and epoxy.

3.3.5 Further attempts

The samples treated as described in the previous section were still not completely sealed and the drying was most likely due to water being transported out, either through the epoxy or between the glass and epoxy (red arrows, figure 3.8(b)). This creates a lowered pressure inside the pore network that pulls on the existing gas volumes in the injection points. These small volumes of gas are a lot easier to stretch than it is to nucleate water vapor from the liquid water. In addition, diffusion of gas from the surrounding enviroment into the sample might have supplied the water with dissolved gas. This dissolved gas requires a smaller pressure change to nucleate gas bubbles than water vaporizing from the liquid phase. This section will describe other attempts to fill the sample without using injection sites and syringes.

As a way of trying to avoid the gas at the injection points, we attempted to use the relatively fast diffusion in the PDMS to our advantage. The idea came from the treatment of hydrogel by Vincent et al. [2012] where one soaks the sample in degassed water. Because of the air inside the sample and the lack of air in the water, the concentration gradient sets up diffusion of air out of the sample and water into the sample. This method would allow us to avoid cutting injection holes in the PDMS and thereby avoid having small volumes of gas in the system. This could enable the system to subject the water to tension and thus recreate conditions close to those in a real tree. In addition, the system might be able to cavitate instead of expanding gas as previously described.

To begin with it seemed that we had trouble with the degassing procedure (table 3.6). Initially, a desiccator connected to a vacuum pump was used. One sample was filled within 6 hours of soaking, but attempts to recreate the same conditions did not yield the same result. After trying several different periods of degassing, we decided to preheat the water. This was done because gas in hot water has a lower solubility than in colder water. Also it might help to get the water boiling, because nucleation of water vapor should have a higher barrier to nucleation than nucleating air from a solution. That is, if the water starts boiling, the pressure should be low enough to separate gas from the water. By preheating the water to between 50 and 70°C, the water boiled rather quickly in the desiccator (less than 30 seconds). However, this did not have any notable effect for the diffusion filling of the samples.

The last attempt, and a sure way to obtain degassed water, was to let it boil at normal pressure for a while. By letting it boil for about 15 minutes and cooling it down in a sealed container, the water should be properly degassed.

When this also failed to yield any different results, diffusion filling of the PDMS samples was abandoned as a viable method for the remainder of the experiments.

A while later it was discovered that the sample that seemed to have been filled using diffusion had a long thin particle, possibly an eyelash or a thin thread, present on the glass or PDMS at the time of mounting the PDMS onto the glass. This might have led the PDMS to not adhere properly around it, and it looked like it created a small thin channel that connected the network to the enviroment outside the sample. This might have been the reason why only that particular sample was filled using this method. Regardless, prior to discovering this, the unreproducibility led us to dismiss this as a viable method. Attempts have been made with different methods of degassing water, but none prevailed, see table 3.6.

A similar approach was tested using a desiccator and a vacuum pump. The idea was that by submerging the sample in water and placing the container into the desiccator, the air inside would expand and be forced out of the pores. It did not fill the sample nor did it saturate the PDMS. This was most likely due to the rigidity of the PDMS, namely that the PDMS resisted the volume expansion or that the PDMS kept the pressure in the pore from being lowered sufficiently.

The conclusion from the development of the PDMS samples was that the fastest to make, and the most stable samples, were the ones treated with epoxy and a cover glass. Most of the results presented in the next chapter where PDMS was used were prepared with this method. The following section will describe the preparation and treatment of the hydrogel sample.

Exp name	Sample	Preparation	Notes
120413a	PDMS13	Test of diffusion filling. Water was degassed using a desiccator and vacuum pump for about 10 min.	The samples appeared unaltered after 24 hours. Believe to be problem with degassing.
120413b	PDMS14	Repeat of previous	Same outcome.
120416	PDMS13	Degassed for 20 min. Minimal activity while degassing. Sealed the sample with no air inside the container.	5 hours room temp, no change. 16 hours at 50°C, the PDMS had saturated and the pores filled with condensation droplets. No change after an additional 48 hours.
*120418	PDMS14	Preheated the water before degassing in desiccator. The water boiled quickly. The sample was then soaked for a few hours.	The result was whitening of the PDMS and small droplets in the pores.
*120419	PDMS13	Saturated sample in degassed water from experiment 120416 (72 hours).	Confirmed that what looked like condensation indeed was that.
120423	PDMS15	Diffusion filling for 1 hour.	Not filled.
*120425	PDMS15	Diffusion filling for 3 hours.	Not filled, slightly saturated PDMS.
*150515a	PDMS15	Diffusion filling for over 24 hours.	Saturated PDMS and condensation droplets in pores, as before.
*120515b	PDMS16	Removed channel connections on one mold (100 pores), made a cast, attempted diffusion filling seven days.	System equilibrate when the PDMS was saturated and pores filled with condensation droplets (about 12-16 hours).
120516a	PDMS15	Put an already saturated sample in an open waterbath inside the desiccator.	It did not yield any results.
120516b	PDMS13	Same as above but with a dry sample.	Same result

Table 3.6: A table of the experiments in which we tried to use diffusion filling and low pressure driven filling of the samples.

3.3.6 Hydrogel

In addition to the PDMS samples, we were given a sample of hydrogel (figure 3.9) from Philippe Marmottant at the Laboratoire Interdisciplinaire de Physique (Université de Grenoble). The hydrogel sample was used in order to study nucleation and cavitation in isolated pores during freeze-thaw cycles at negative pressures [Vincent et al., 2012]. This sample had isolated pores of uniform size with radii of 50μm, heights of 100μm and the centers of each pore was 220μm apart. The technique used for creating this type of sample was similar to that used for the PDMS samples, but instead of mounting the hydrogel with a desired pattern on a glass slide one, uses an additional flat sheet of hydrogel.

Hydrogel is a material composed of polymers that adhere to each other when exposed to UV radiation. The resulting material is stiffer than PDMS while having similar diffusive properties. When it is saturated, this results in higher evaporation rates at its surface.

To fill the hydrogel sample, we used degassed water to allow for diffusion as described in the previous section. This subjects both the gas in the empty sample and the water surrounding it to a concentration gradient. As the gradients point in opposite directions, air diffuses out and water diffuses into the sample. After a few attempts with the desiccator and vacuum pump, boiling the water became the method used. The sample was then soaked for one night. To mount the sample in the setup, the hydrogel was removed from the water and the surfaces were quickly dried with tissue paper. Without delay, the sample was placed between a glass slide and a plexiglass slide with a 7mm diameter hole in the middle (figure 3.9). This was done in order to slow down the cavitation rate by having evaporation at only one surface. This allowed some pores to freeze before cavitating which was necessary due to the high cavitation rate compared to the rate of freezing.

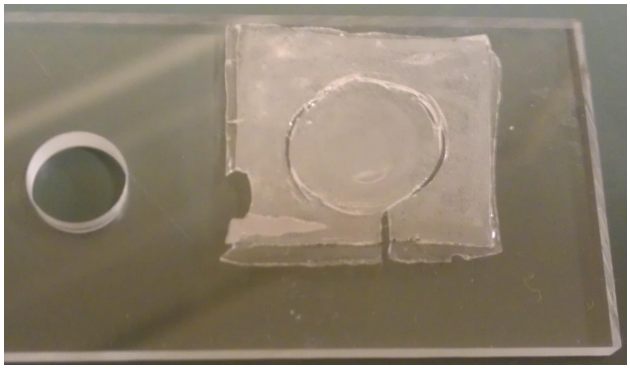

Figure 3.9: A picture of the hydrogel sample resting on top of the plexiglass slide. The hole in slide has a diameter of 7mm. The hydrogel sample in the image is broken and we see the fracture forming a circle that connects to the edge. This happened after the experiment 120601 (table 3.7) was completed. The size of the plexiglass slide is 75×25mm.

Exp name	Sample	Preparation	Notes
*120503	HYD	Water degassed by desiccator and vacuum pump. Sample placed between two glass slides.	The sample was only partially filled, and it was difficult to observe anything due to the use of a macro lens.
*120505	HYD	Same filling procedure as above. Hydrogel placed between two glass slides.	Using a microlens gave a better view of the sample, and both cavitation and possibly some freezing was observed. However, a higher zoom was needed and water trapped between the sample and the glass made observations difficult.
120522	HYD	Degassed water in desiccator again.	The same microscope lens was used as above. Sample was clearly not filled properly. That was determined by the number of menisci observed in the pores.
120523a	HYD	Same as above.	Sample did not seem properly filled.
120524	HYD	Boiled water. Filled sample for about 1 hour and used a plexiglass slide with a hole in the middle as described in the text.	The sample was poorly filled.
*120529	HYD	Boiled water and let the hydrogel soak overnight.	Sample was properly filled and both cavitation and freezing was apparent.
*120531	HYD	Same as above.	Better stability on the lens afforded higher contrast due to the sensitivity of the lens.
120601	HYD	Same as above	Failed attempt to recreate results from 120529 due to that the lens was knocked out of focus when the box was removed from the freezer.

Table 3.7: A table of the experiments conducted using the hydrogel sample.

Chapter 4

Results

In this chapter, the results from the PDMS and hydrogel experiments will be presented. In addition, some observations done during the experiments using capillary tubes have been included. The chapter is devided according to sample type. Firstly, observations of freezing and thawing of connected pores in PDMS and in capillary tubes are presented. The drying of the PDMS network has been included. Lastly, the observations of freezing, thawing and cavitation in the isolated pores of the hydrogel sample are presented.

A list of the experiments that yielded results, including some additional observations, is presented in table 4.1.

Table 4.1: A list over the experiments conducted using the setup described in section 3.2. NrC denotes the number of freeze-thaw cycles, T_f the freezing temperature of the consecutive cycles and t_{dry} the time from the start of the experiment to the onset of drying. The water was distilled in all the experiments presented.

Exp name	**Sample**	**NrC**	T_f	t_{dry}	**Notes**
120119	CAP01	4	-09.6 -11.1 -11.5 -11.5	-	Gas forced out of solution every cycle. Tube froze from edges to center.
120208	PDMS01	1	-13.3		Tubes cut and sealed with epoxy, partially filled network. Ice matured over a few seconds. Some pockets of water freeze a little later. Gas released on thawing.
120222a	PDMS03	-	-	10m	Sealed with epoxy after injection.
120222b	PDMS03	-	-	2h16m	Let shut luer-lock valves in. Completely dry in 15h.
120224	PDMS03	-	-	1h3m	Double glass and silicone with reservoir. About 25% dried after 2h3m.
120315	PDMS08	3	-21.6 -20.9 -21.2	-	Confirmed it was full and saturated. Can see maturation of ice crystals for some seconds. No observable gas on thawing.
120320	PDMS09	2	-15.8 0	7h5m	Hint of two-stage freezing. Freezes from left to right. Ice maturation. Not melted properly, so ice was already present on the second cycle. Nucleation site.
120322	PDMS 10	3	-13.0 -12.9 -14.0	10h19m	Observed two-stage freezing and ice maturation. Some gas release observed on third cycle. About 70% dry after 23h30m.
120330a	PDMS12	3	-15.9 -15.8 -15.7	-	PDMS treated with glass and epoxy after hot bath. Pictures taken with microscope lens. Observed two-stage freezing and some gas release every cycle. Tried to record drying over five days. None observed in the field of view.
120404	PDMS12				Continuation of previous experiment, but changed the field of view to find a meniscus. No changes over 24 hours even though about 50% of the pore network was dry (observation made in microscope).
120405	PDMS11	-	-	2h30m	Hot bath, glass and epoxy. A drying experiment with a microscope lens. Observed are was dry in 6h30m.
120418	PDMS14	-	-	36m	About 100% dry after 12h10m. Might be failed diffusion.
120419	PDMS13	-	-	-	Saturated and condensed droplets in pores. Confirmed by drying. Clearly dries from edges.
120425	PDMS15	-	-	-	Diffusion filling, slightly saturated and some condensation droplets.

Continued on next page

Table 4.1 – *Continued from previous page*

Exp name	**Sample**	**NrC**	T_f	t_{dry}	**Notes**
120503	HYD	-	-	-	Hydrogel sample through macro lens. Cavitation and freezing indistinguishable. Ice formed between the glass and hydrogel.
120505	HYD	-	-	-	Macro lens with zoom. Cavitation and freezing still indistinguishable. Experiment showed activity over ten days in the freezer.
120515	HYD	-	-	-	Drying of hydrogel. Does not seem to be filled properly.
120515a	PDMS15	-	-	-	Tested diffusion filling for appxomiately 24 hours. Not filled.
120515b	PDMS16	-	-	-	Removed channels from one mold to get isolated pores in PDMS. Observed saturation of PDMS and vapor in pores after 12 and 16 hours hours in hot bath. No change after seven days.
120515c	PDMS02				
120516c	PDMS02	-	-	90s	Injection, no saturation or sealing. Sample started drying very quickly.
120519	CAP02	-	-18.4 -12.0 -22.6	-	Freezing temp listed from largest to smallest tube. All tubes broke on freezing. More gas on thawing the larger the tube. Also, the largest tube formed a destinct band of bubbles on freezing.
120523b	PDMS17	3	-	-	Higher framerate camera (82fps) to enhance time resolution to study two-stage freezing. The front shows a higher intensity (brightness on image) than stable ice. Covered the visible are in 0.15 and 0.11 seconds on the second and third cycle. Thawing shows gas on third cycle. Some menisci move on thawing.
120529	HYD	-	-	-	About 150 pores were visible. Roughly 30 froze, the rest cavitated. Fast cavitation on thawing. Some look like ice-gas, some show clear ice-water-gas. All cavitated quickly after thawing.
120531	HYD				Better stability than 120529 due to the use a support under the lens. Observed cavitation and freezing.
120607	PDMS18	1	-16.5	-	Saturated and treated with epoxy ang cover glass. High time resolution camera and microscope lens.

4.1 PDMS & capillary tube experiments

4.1.1 Two stage freezing

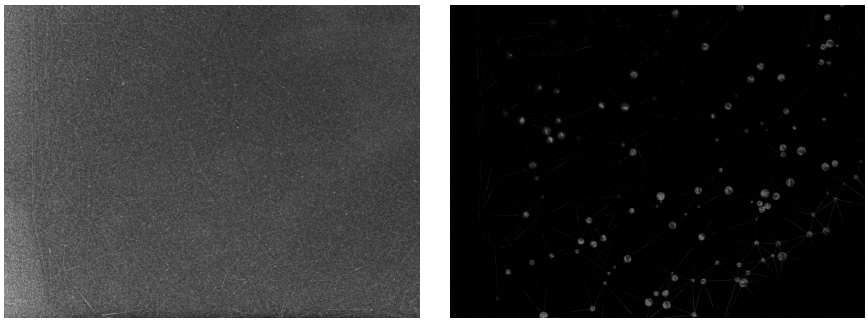

(a) t=0

(b) t=156ms

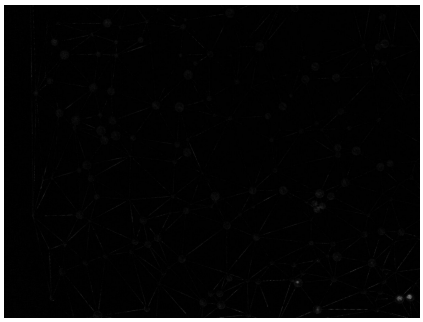

(c) t=313ms

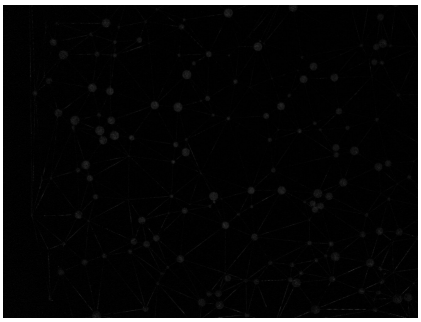

(d) t=3000ms

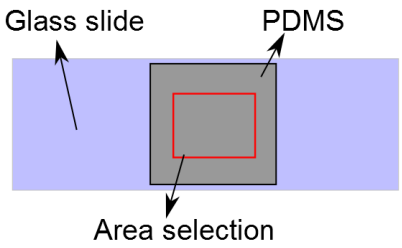

(e) A schematic showing the approximate field of view.

Figure 4.1: Two stage freezing in a connected pore network in PDMS. The water has a temperature is -12.9°C. The first photograph is the untreated image from the experiment just prior to freezing. This photograph has been subtracted from the following photographs to reduce the noise from the saturated PDMS matrix seen in the first. The pictures are from the second cycle of experiment 120322 and show an area of 17.0×12.8mm (photolens, minimum zoom) of sample PDMS10 (300 pores).

The pictures in figure 4.1 show a feature common to the PDMS samples that were frozen. The pictures show a field of view that is 17.0×12.8mm, which is approximately 50% of the pore network of the sample PDMS 10 with 300 pores. The photographs depict freezing on the second cycle of experiment 120322 (table 4.1).

The picture shows that the network started to freeze at -12.9°C and a first wave of ice covered the visible area in approximately 156ms (figure 4.1(b)). After another 157ms the ice had relaxed to a barely visible state (figure 4.1(c)) which matured and stabilized after approximately 3 seconds (figure 4.1(d)).

Note also that there seemed to be some directionality of the first wave of ice. In figure 4.1(b) there is little bright ice in the upper left and lower right corner of the picture. In the next image (figure 4.1(c)) we see some of the bright ice in the lower right corner. This indicates that the wave of ice in this stage of freezing went from upper left to lower right. Also, the first wave of ice appears brighter on the images that the stable ice.

Image analysis was done on the event shown in figure 4.1 to measure the characteristic times of the two stages of freezing. The first plot (figure 4.2(a)) shows the average intensity through time and the second plot (figure 4.2(b)) shows the average intensity where the peak corresponding to the first wave of ice has been isolated. Note that the average was taken after subtracting a background image to reduce noise, hence the low initial intensity.

The characteristic time parameter of the first stage of freezing was defined as the time between the two points where the intensity had the value of the minimum following the peak, i.e. the differnce in time between the intersection and the tangent of the black and red line in figure 4.2(b). The second time parameter was found by fitting an exponential function of the form

$$I = I_0 - \Delta I e^{-\frac{t}{\tau_2}} \tag{4.1}$$

Where I_0 was the intensity at the minimum following the peak and ΔI is the difference between the value of the intensity where the blue curve flattens out (maximum I for the blue curve) and I_0.

This has been plotted in red in figure 4.2(a). A logarithmic plot of this equation turned out to be highly sensitive to the noise in the images. The method used for fitting was to minimize the absolute value of the difference between an estimated intensity and the one measured from the images measured. For the data presented in 4.2, the time paramters were $\tau_1 = 0.28$ seconds and $\tau_2 = 3.25$ seconds.

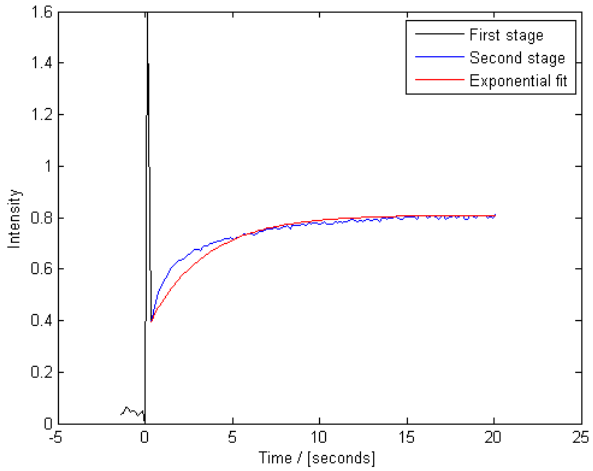

(a) A plot of the average intensity through time for a two-stage process.

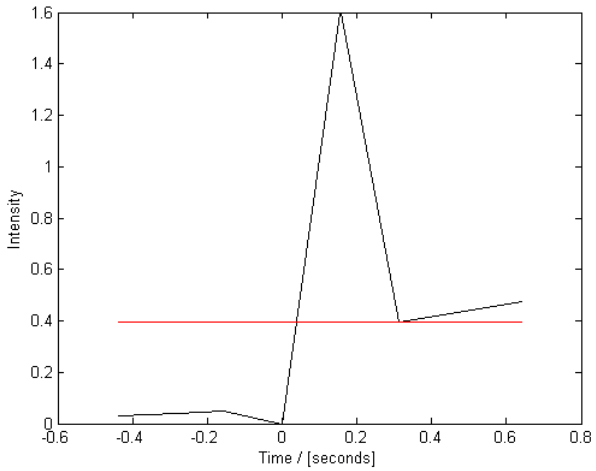

(b) A plot of the average intensity through time for the first stage of freezing.

Figure 4.2: The figure (a) shows the average pixel value of the images through time. The black line corresponds to the first stage of freezing and blue is the second. Figure (b) is a plot of the average intensity of the first peak in (a). The red line indicates the width used for defining τ_1. The data is collected from the same event as depicted in figure 4.1.

The peak in figure 4.2(b) is only visible over two frames, which limits the measurement accuracy of τ_1 by the time resolution of the pictures, however, it will demonstrate some aspects of the process and will be used as a measure

when comparing systems later. In the presentation of results were similar analysis is included, only the parameters τ_1 and τ_2 will be taken into account when characterizing the duration of the two stages of freezing. Also, the color coding of the plotted datasets will be consistent in the following image analysis.

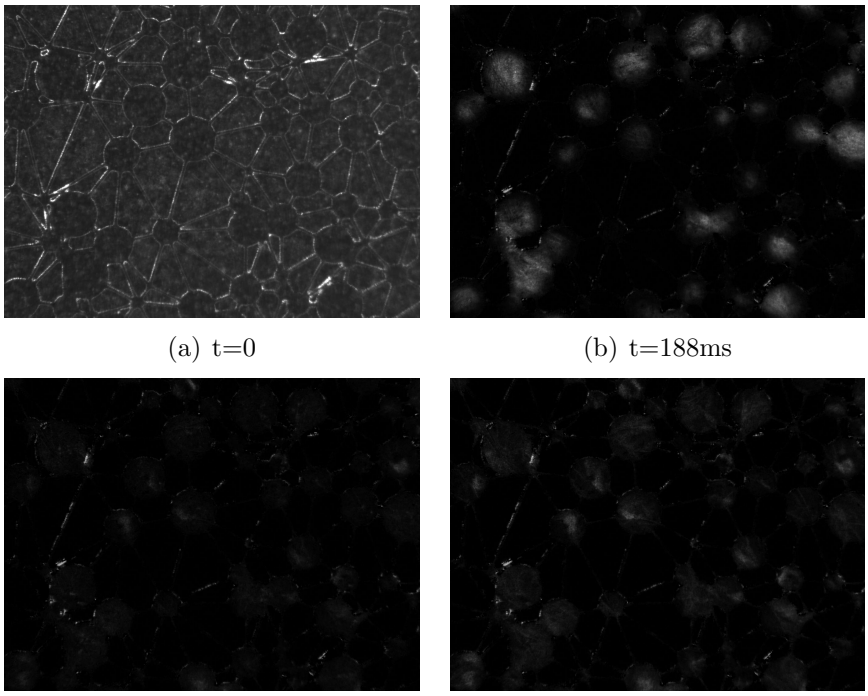

(a) t=0 (b) t=188ms

(c) t=359ms (d) t=3563ms

Figure 4.3: Two stage freezing photographed using a microscope lens (2×). The temperature of the water is -15.7°C. Pictures taken from the third cycle of experiment 120330 and show a field of view that is 3.40×2.56mm of sample PDMS12 with 3000 pores. In this figure, the first image is the original, taken from the experiments. The following images are the result of subtracting the first. This was done to separate out the changes, i.e. the ice, between the first and subsequent photographs.

The same behavior was observed when using a microscope lens, figure 4.3. Here, the background noise from the saturated PDMS has been greatly reduced due to the shallower depth of field of the lens (microscope lens, 2×). These pictures were taken from the third cycle of experiment 120330 from table 4.1. The sample (PDMS12) has 3000 pores. Again, the visible area (3.40×2.56mm) is covered with ice after 188ms (figure 4.3(b)). The next frame is after a total time of 359ms where we see that the ice has not disap-

peared, but it was a lot less visible (figure 4.3(c)). Subsequently, it matured until approximately 3563ms had passed and remained stable, figure 4.3(d). Again, the ice of the first wave appeared brighter than the ice of the second wave, even after it had matured and stabilized. No observable directionality of the first ice was observed, most likely due to the low time resolution.

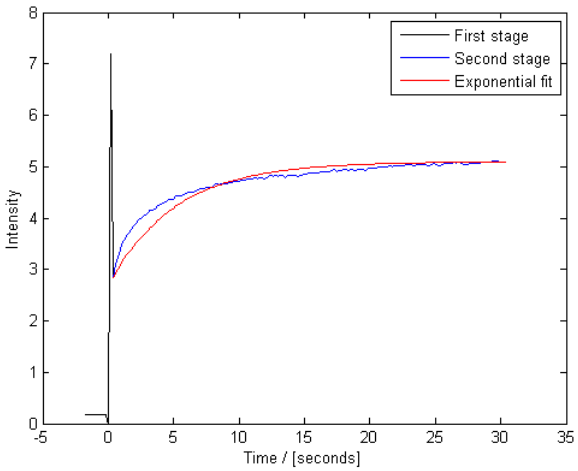

(a) A plot of the average intensity through time for a two-stage process.

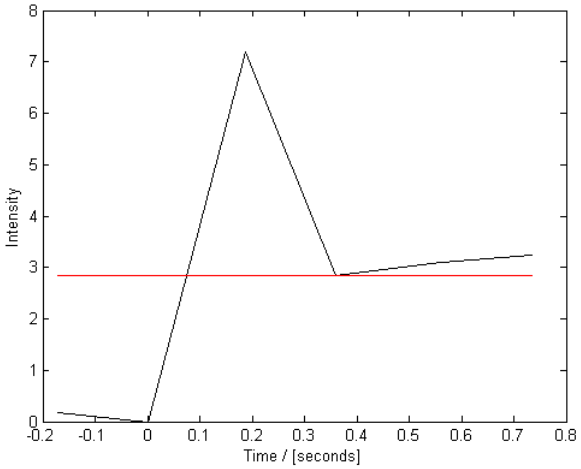

(b) A plot of the average intensity through time for the first stage of freezing.

Figure 4.4: The figure (a) shows the average pixel value of the images through time. Figure (b) is a plot of the average intensity of the first peak in (a). The data is collected from the same event as depicted in figure 4.3.

The image analysis of the data from this cycle of the experiment (120330) is shown in figure 4.4. The characteristic time of the first wave of ice was $\tau_1 = 0.29$ seconds. This compares well to the value from the previous experiment ($\tau_1 = 0.28$). The second characteristic time parameter for the growth of stable ice was fund to be $\tau_2 = 5.09$ (previous $\tau_2 = 3.25$).

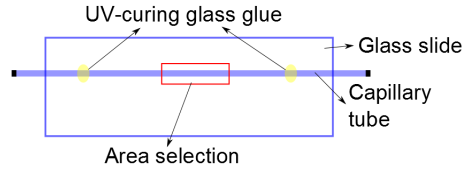

(a) An approximate field of view for the capillary tube.

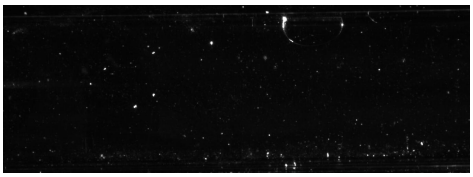

(b) t=0

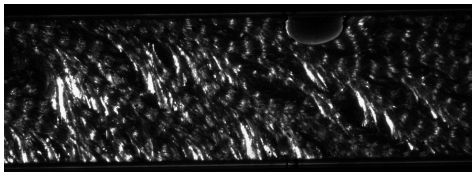

(c) t=2590ms

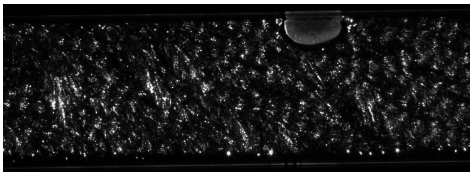

(d) t=7800ms

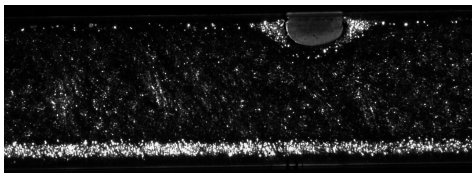

(e) t=12980ms

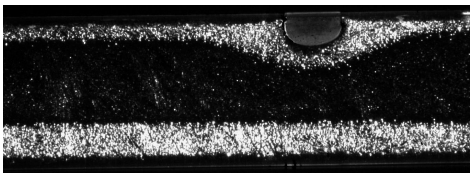

(f) t=18190ms

Figure 4.5: Images showing two stage freezing in a capillary tube. Here, the tube is 4mm wide (height of image) and 0.2mm thick (along an axis normal to the page). The temperature is -11.1°C. The pictures are taken from the second cycle of experiment 120119 (table 4.1) using a photolens. The bright ice in (f) eventually covers the entire sample after about 27 seconds as shown in a plot of the average intensity of the images through time (figure 4.6(a)).

Similar behavior was also seen when conducting the same experiment on water confined in a capillary tube, figure 4.5. The pictures are taken from the second cycle of experiment 120119 (table 4.1) where a photolens has been used. Prior to the onset of freezing, the water was liquid at a temperature of -11.1°C. Then, some form of dendritic ice formed and covered the entire height of the sample (4mm) after 2590ms (figure 4.5(c)). This ice became less apparant after 7800ms (figure 4.5(d)) and continued to fade away as stable ice started growing from the sides of the tube (from the top and bottom edge in the pictures) (figures 4.5(e) and 4.5(f)). The bubble visible in the upper

part of the tube was gas separated out on thawing in the previous cycle.

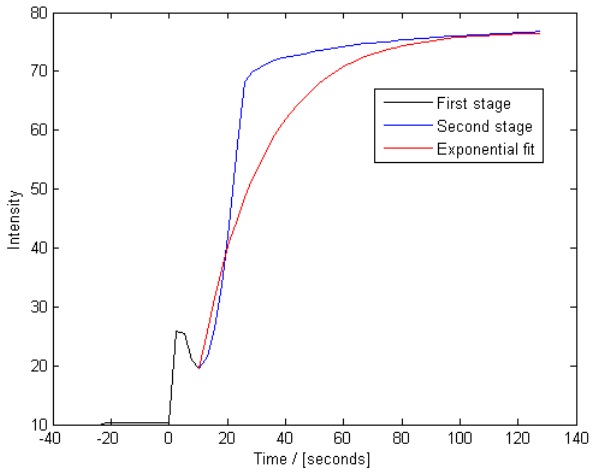

(a) A plot of the average intensity through time for a two-stage process.

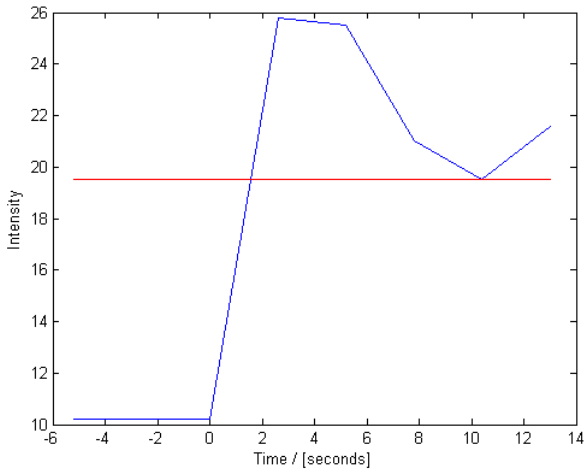

(b) A plot of the average intensity through time for the first stage of freezing.

Figure 4.6: The figure (a) shows the average pixel value of the images through time for the capillary experiment from figure 4.5. Figure (b) is a plot of the average intensity of the first peak in (a).

A significantly slower process is depicted in the capillary tubes (figure 4.5) compared to the two previous experiments with PDMS (figures 4.1 and 4.3). The characteristic time parameters reflect this as $\tau_1 = 9.0$ and $\tau_2 = 12.55$, which compared to the values from the two previous experiments is about 32

times higher for the first stage of freezing and about 2-3 times higher for the second.

The values of τ_1 indicated that what limits the freezing rate of the first stage of freezing was significantly altered between the two model systems. This was most likely due to the difference in the total volume of water in the two types of systems.

The difference in the second parameter is likely coupled to the difference in production and conduction of latent heat between the two types of systems. This is consistent with Sun and Scherer [2010] who determined that heat conduction is a factor controlling the growth rate of ice. The PDMS system allows for a faster heat conduction than the capillary tube which allows the ice to grow faster. This will be discussed further in chapter 5.

The discrepancy in τ_2 between the two PDMS systems most likely explained by the same reasoning. The first sample had $\tau_2 = 3.25$ (4.1) and contained less water in its 300 pores than the one depicted in figure 4.7 with 3000 pores ($\tau_2 = 5.09$). This means that the latter sample produced more latent heat which resulted in a slower growth rate and thus a larger value of τ_2.

To study the two-stage behavior of freezing more closely in a PDMS network, a camera with higher timeresolution was used (82fps) with the photolens. This is shown in figure 4.7. The images show the continued freezing front going from left to right over an area that is 18.8×12.0mm. The entire area was filled with ice after approximately 80ms. We see that the freezing spread from pore to pore rather than as isolated nucleation events in pores and that the ice appeared to be somewhat brighter near the freezing front.

The series of images from this two-stage freezing was analysed in the plots in figure 4.7. By averaging the intensities over every column in each picture, we got the mean intensity as a function of position (left to right). A plot of two of the average intensities is displayed in figure 4.7(e). By manually setting a threshold value of 1 for the average intensity (corresponding to the value 1 on the y-axis of figure 4.7(e)), the position of the front could be estimated. This is shown in figure 4.7(f). By fitting a linear curve to the datapoints, an estimate of 238mm/s, or 0.24m/s, was found.

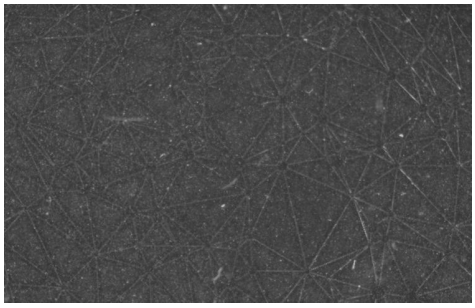

(a) t=0

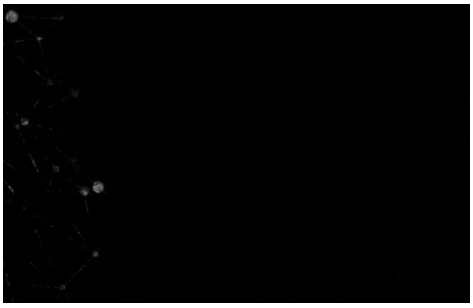

(b) t=10ms

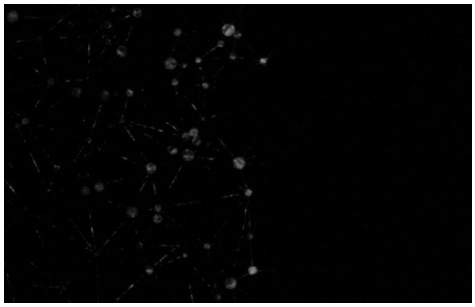

(c) t=30ms

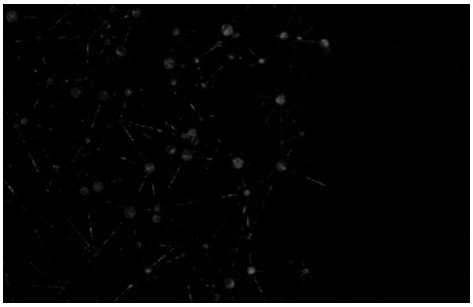

(d) t=50ms

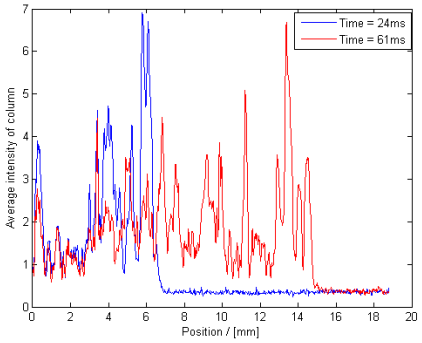

(e) Plot of the average intensity of columns for t=24 and t=61ms.

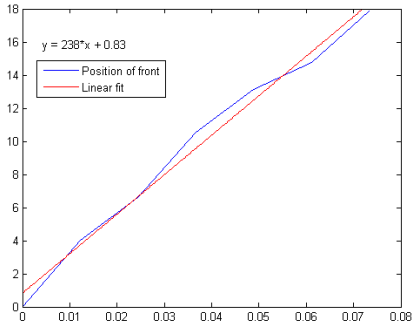

(f) Plot of the position of the ice front as a function of time.

Figure 4.7: Pictures showing the freezing front of the first stage of ice formed in a PDMS network. A background images has been subtracted from these images to remove the background noise from the saturated PDMS matrix. The images are taken from the first and only cycle of experiment 120607 (table 4.1) using a photolens. The water froze at a temperature of -16.5°C and the pictures show an area that is 18.8×12.0mm. The plots (figures (e) and (f)) show the results from the image analysis where the velocity of the ice front was measured.

4.1.2 Release of gas on melting

In several experiments, bubbles could be observed on thawing over more than one cycle. The pictures in figure 4.8 are taken from experiment 120607 (table 4.1) using a microscope lens (×5). The sample is PDMS18 (300 pores) of which we see an area of 1.50×0.96mm. When the sample started thawing, small bubbles that were trapped in the ice became appearent (figure 4.8(a)). In this experiment, the bubbles seemed uniformly distributed and they varied in size. After 6.33 seconds, the smaller bubbles had either redissolved, or coalesced, into larger bubbles (figure 4.8(b)), and after a total of 16.01 seconds after the first image, we see that some of the bubbles were released from the ice (figure 4.8(c)).

The number of bubbles that were released from the confinement of the ice was significantly smaller than the total number of bubbles trapped in the ice in figure 4.8(a). This indicated that some smaller bubbles either redissolved rather quickly upon thawing or coalesced into larger bubbles. The latter seemed unlikely as we would have expected the remaining bubbles to grow. This was not observed. We also note that bubbles were released in all three differently sized pores (figure 4.8(a) and 4.8(b)). In this, and subsequent experiments showing thawing in PDMS, all bubbles redissolved. Some became obscured by either a channel or a pore wall, but no build-up of stable bubbles were observed.

Figure 4.9 shows the thawing of the third cycle from experiment 120330 (same experiment as shown in figure 4.3). The series of pictures were cropped from the original to show sequential photographs of the thawing process where small bubbles, indicated by red rings, were separated out of the ice and drift upward. The area shown is 0.92×0.86mm. Using this lens (photolens), gas was evident in most of the larger pores in the sample. Even though there appeared to be fewer bubbles in this experiment than the one presentet in figure 4.8, this showed that gas was indeed released over consecutive cycles. Also, as in figure 4.8, we observed redissolution of the gas bubbles.

Similar behavior was visible in experiment 120119 using the capillary tubes (table 4.1). Figure 4.10(a) shows a stable bubble which was formed from many small bubbles released from the ice on thawing on the first cycle. The bubble grew over consecutive cycles and coalesced with another stable bubble from figure 4.10(b) to figure 4.10(c). The bubble seen in figure 4.10(a) was the same bubble that was seen trapped in the ice in figure 4.5.

This demonstrated that gas was released over consecutive cycles, however,

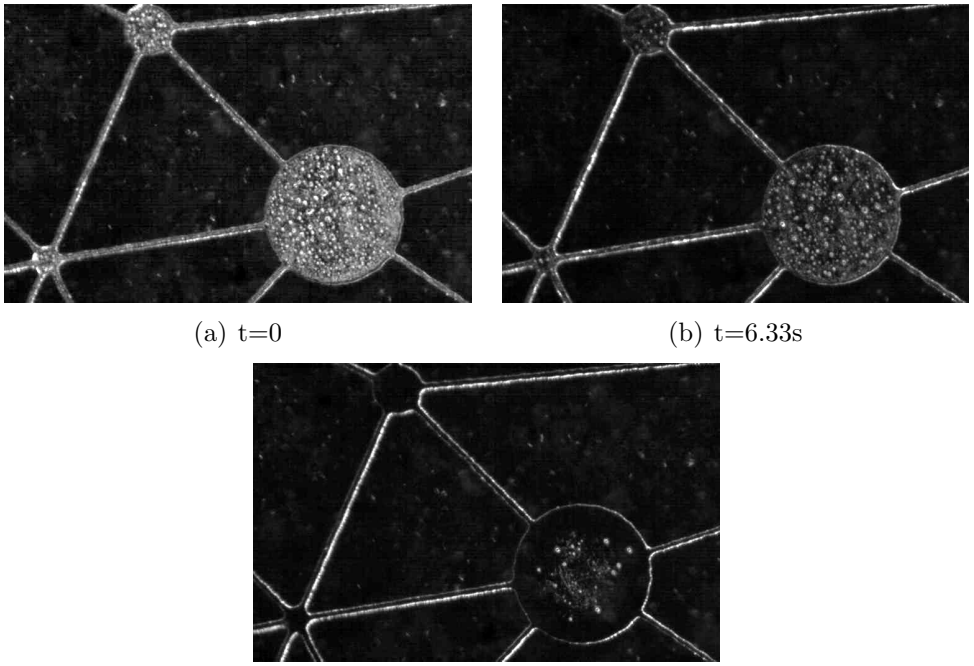

(a) t=0 (b) t=6.33s

(c) t=16.01s

Figure 4.8: Images showing the release of gas on thawing from three pores in PDMS18 from the first cycle of experiment 120607 (table 4.1). The images are taken with a microscope lens (5×) and show an area that is 1.50×0.96mm. The contrast has been enhanced from the original images using ImageJ.

the volume contained in the capillary tube might not have been constant for the duration of the experiment. The capillary tubes were filled at 1atm pressure and sealed with a soft wax at the ends. On freezing, the seals might have moved, which would explain how non-compressible water allowed bubbles to grow. Had the seals not moved, the amount of released gas would not be able to compress the water and form a stable bubble. This will be discussed further in chapter 5.

Figure 4.11 shows the largest of the three capillary tubes (experiment 120519, table 4.1) after freezing. In this case, the goal was not to capture two-stage freezing, but rather the evolution of stable bubbles over consecutive cycles for capillary tubes of varying sizes, as seen in experiment 120119. Unfortunately, all capillary tubes broke when they froze on the first cycle, but the largest tube displayed a band of bubbles trapped in the ice just above the middle. This non-uniform distribution of bubbles was not observed when studying the gas release on thawing in a pore network. In the PDMS networks, we observed that the release of gas was not from the center or edges of the pores,

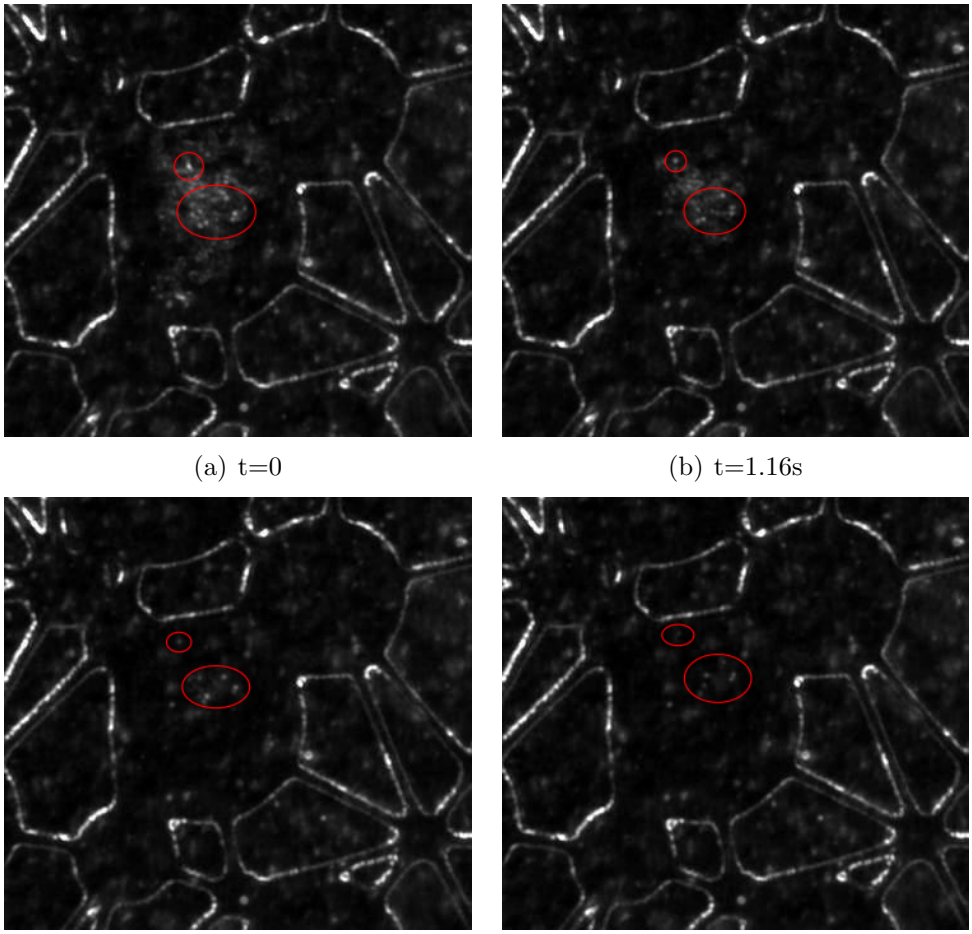

(a) t=0 (b) t=1.16s

(c) t=2.33s (d) t=3.50s

Figure 4.9: Images showing the release of gas on thawing from some of the pores from the third cycle of experiment 120330, table 4.1. The small red ring above the larger one follows one big bubble as it is released from the ice and drifts upwards while it redissolves. The larger ring follows a cluster of bubbles that is freed from the ice. Here we note that some bubbles redissolve completely within seconds. The images are cropped and cover a width of approximately 0.92mm and a height of about 0.86mm.

but spread uniformly over the entire pore. The difference between the two systems will be discussed further in chapter 5.

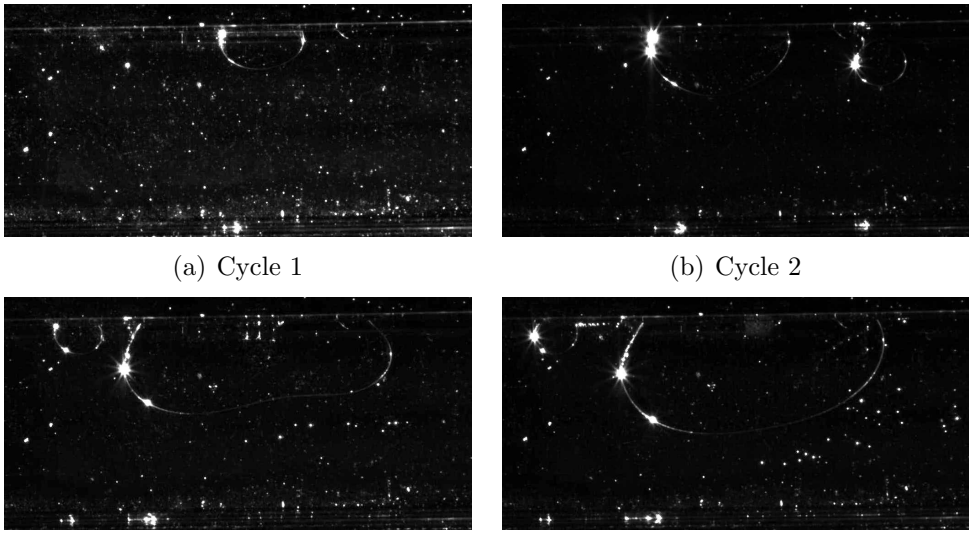

(a) Cycle 1 (b) Cycle 2

(c) Cycle 3 (d) Cycle 4

Figure 4.10: Images showing the growth of stable bubble by gas released on thawing over four cycles in a capillary tube (experiment 120119, table 4.1). The pictures are 4.2mm high, and the height and depth (normal to the page) of the capillary tube is 4mm and 0.2mm respectively, and they are 100mm long.

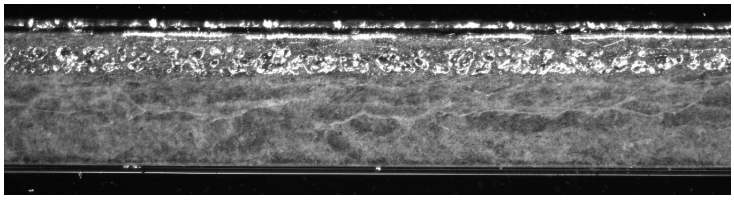

Figure 4.11: A picture taken after freezing of the largest of the three capillary tubes from experment 120519 (table 4.1). The largest capillary tube has a distinct band of bubbles formed just over the central axis that runs the length of the tube. Note: in this experiments, all capillary tubes burst on freezing, so the tube seen here is actually broken. The tube is 0.2mm thick (along axis normal to the page), 4.0mm wide and 50mm long.

4.1.3 Drying & pinch-off bubbles

Prior to the drying of the pore network, the PDMS matrix desaturated and became transparent (figure 4.12). On drying, we observed that the gas that replaced the lost volume of water emanated from the upper left corner of the images (figure 4.12(a)). Further, the volume of gas spread through the sample by expanding into neighbouring pores through the channels connecting them. Nucleation of gas in isolated pores was not observed, indicating that the pressure in the system was above the vapor pressure in the system when the gas was present. The reason for why the pressure did not drop below the vapor pressure was that the expanding gas relaxed the pressure before the pressure could become low enough to nucleate gas bubbles from the water. This will be discussed further in chapter 5.

On closer inspection of idividual pores, an unexpected observation was made. This is depicted in figure 4.12(c) where we see a pore with several small bubbles. This phenomenon was observed on several occasions. These types of bubbles were observed to form sequentially when a pore was filled with gas. After forming two or more bubbles, they coalesced and formed one large bubble that eventually grew and filled the entire pore before the meniscus continues through a connected channel. A sequence of images displaying the evolution of such bubbles is shown in figure 4.13. The pore was fed gas from one channel (top left).

This behavior has been attributed to a pinch-off effect similar to that seen in other microfluidic systems. Pinch-off bubbles are formed when a fluid flows through a choke point. The observations in this experiment are consistent with previously described observations of the pinch-off effect [Dollet et al., 2008].

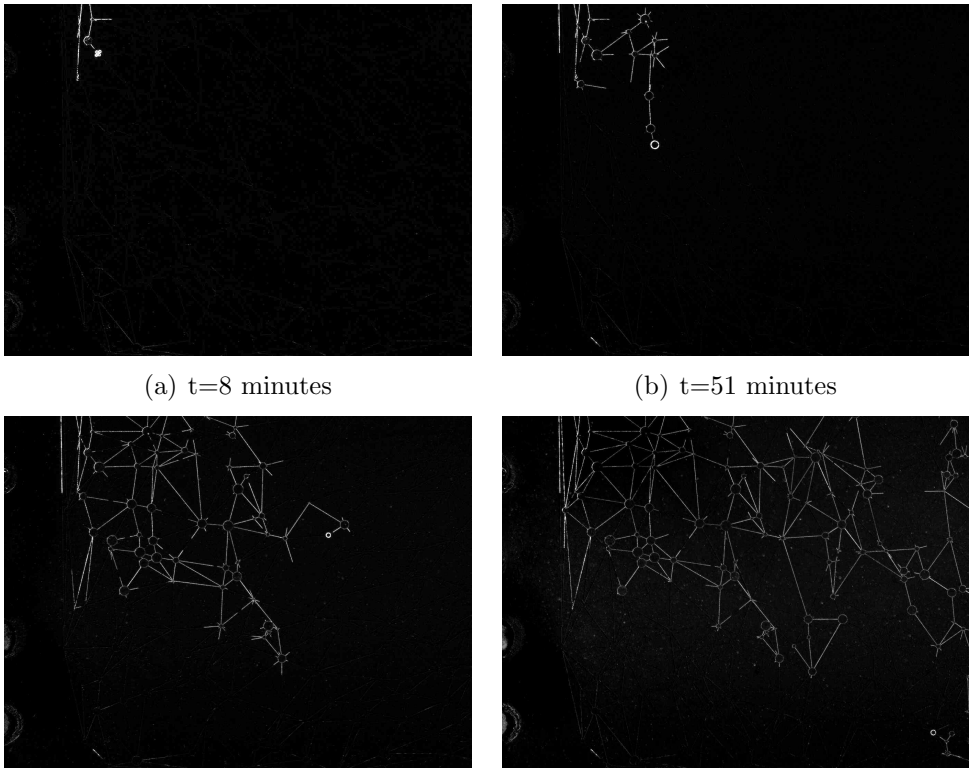

(a) t=8 minutes

(b) t=51 minutes

(c) t=4 hours 6 minutes

(d) t=11 hours 47 minutes

Figure 4.12: Images showing the early stage of drying and a selection of images taken during the process. The onset of drying was, after three freeze-thaw cycles, 10 hours and 20 minutes after the experiment started. The times listed for the images are relative to the onset meaning that the onset of drying is t=0. The sample was between 70-80% dry after a total of 13 hours. The images depict sample PDMS10 from experiment 120322 (table 4.1) and show an area of 17.0×12.8mm (photolens). The images are processed by first subtracting a background image taken prior to the onset of drying. After that, the contrast was increased using ImageJ.

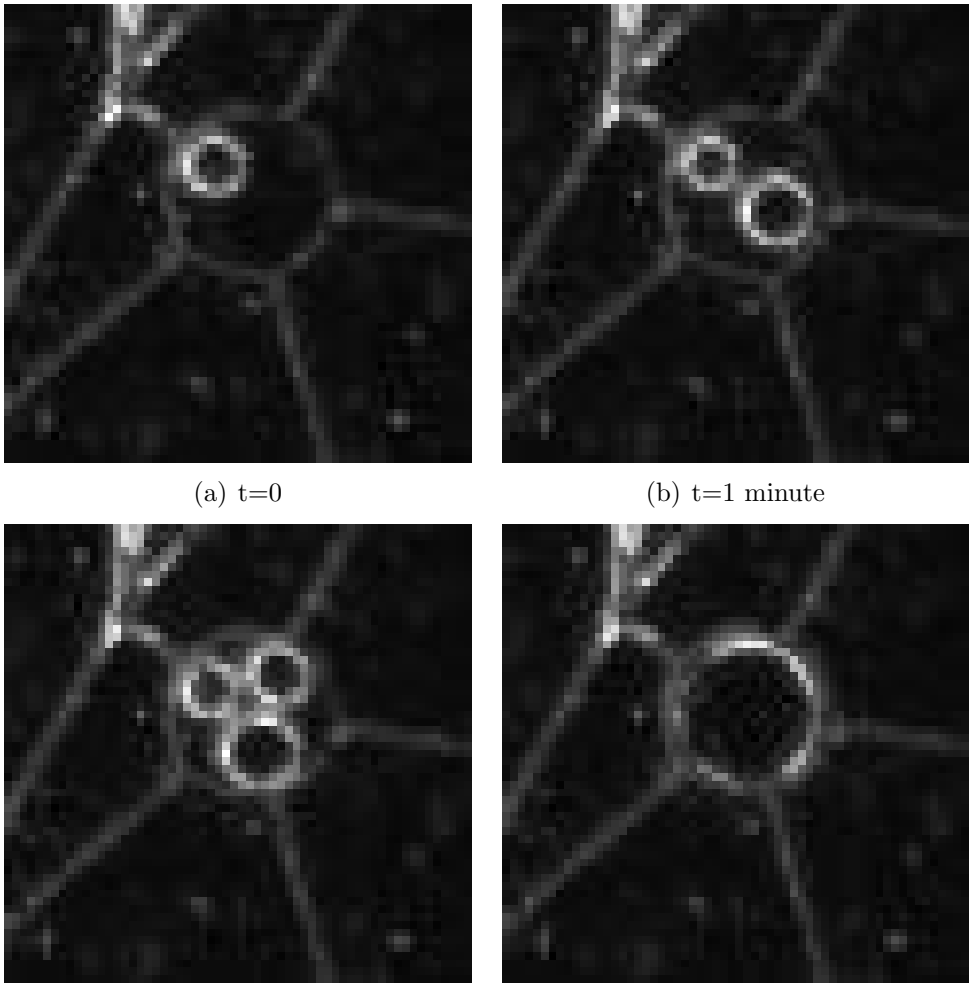

(a) t=0 (b) t=1 minute

(c) t=2 minutes (d) t=3 minutes

Figure 4.13: Pictures showing the evolution of a pore being filled sequentially with three small bubbles that coalesce into one large bubble. The images are from experiment 120322 table 4.1 and show a pore with radius of approximately 130μm.

4.2 Hydrogel

4.2.1 Freezing & cavitation

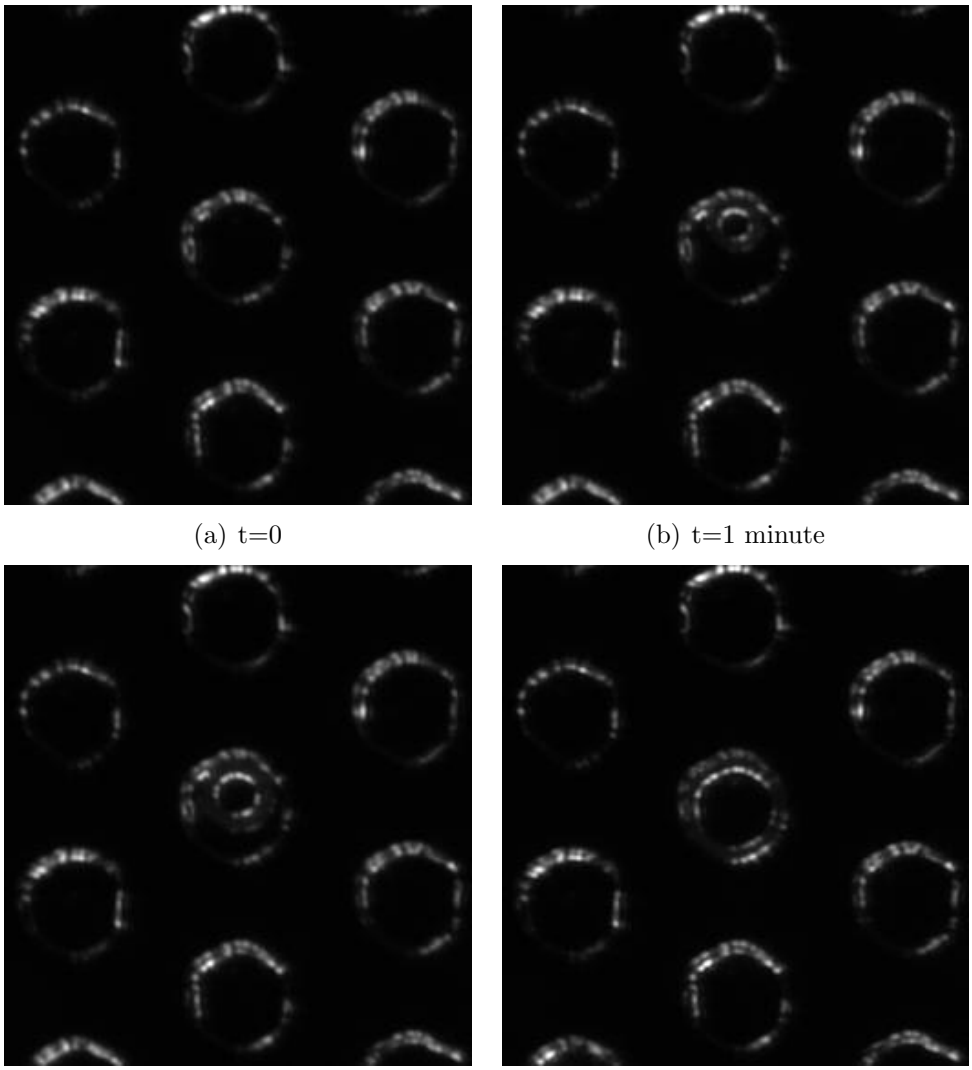

(a) t=0 (b) t=1 minute

(c) t=4 minutes (d) t=17 minutes

Figure 4.14: Pictures showing the evolution of a cavitating pore in hydrogel. The images are from experiment 120529 table 4.1 and the pores have a radius of 50μm.

The experiment presented here (120529, table 4.1) was conducted on the sample of hydrogel with a uniform size distribution of isolated pores, where

the radius of the pores were 50μm. In the experiment, three distinct behaviors were noted prior to, and while it was subject to freezing. The first was cavitation (figure 4.14). The pictures are taken using a microscope lens (5×). The first picture shows a section with seven waterfilled pores (figure 4.14(a)). In the second picture (figure 4.14(b)), a gas bubble has nucleated in the center pore. It continued to grow (figure 4.14(c)) and the pore was dry by figure 4.14(d). The entire process took roughly 17 minutes, but the time from cavitation occured until the pore was dry varied in the experiment between 4-20 minutes.

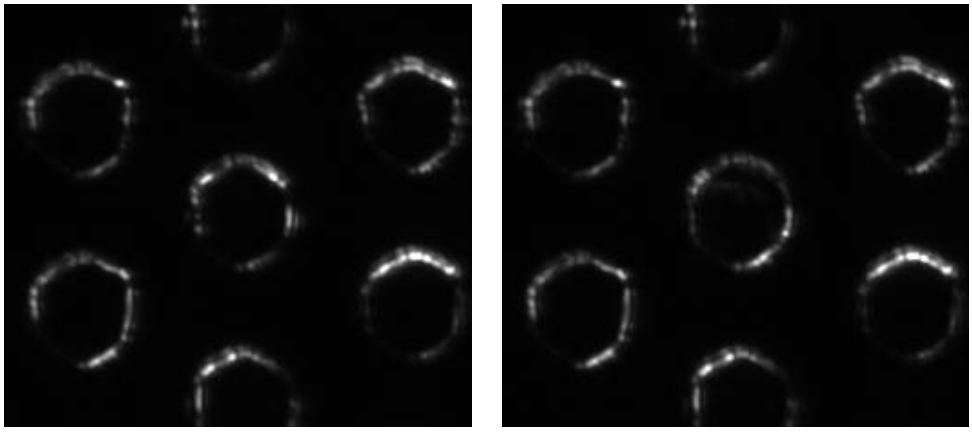

(a) t=0 (b) t=1 minute

Figure 4.15: The pictures show freezing of the center pore. The images are from experiment 120529 (table 4.1) where a hydrogel sample was used where the pores have a radius of 50μm.

The other two behaviors observed in the hydrogel experiment were two different modes of freezing. The first mode is shown in figure 4.15. The first image (figure 4.15(a)) shows a waterfilled pore at approximately -25.8°C. In the next image the pore is frozen (figure 4.15(b)). The ice is hardly visible, but note the change in the pore wall of the center pore as opposed to the surrounding pores. Also, a slight difference in the upper left part of the pore which looks like a horizontal line or stria in the ice.

The second mode of freezing was similar to the first, but it continued to mature over a period of about an hour (figure 4.16). The first picture (figure 4.16(a)) shows a water filled pore that froze in the next picture (figure 4.16(b)). Subsequently, after a period of 26 minutes (figure 4.16(c)) the ice had gradually matured and continued doing so until approximately 51 minutes (figure 4.16(d)).

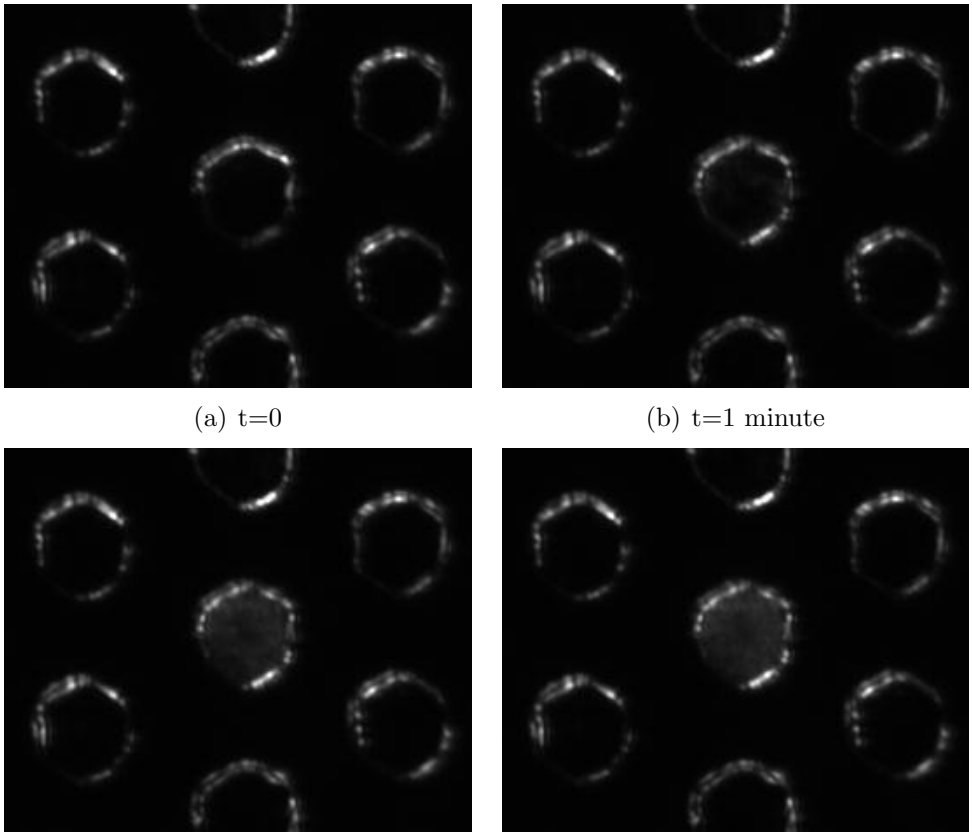

(a) t=0 (b) t=1 minute

(c) t=26 minutes (d) t=51 minutes

Figure 4.16: The pictures show freezing and subsequent maturation of ice in a pore. The images are taken of the hydrogel sample from experiment 120529 table 4.1. The pores have a radius of 50μm.

A plot of the number of cavitated (red) and frozen (blue) pores is shown in figure 4.17. In this plot, the pores that froze with dark ice (black) and bright ice (cyan) are differentiated. The total number of frozen pores is shown (blue). From the plot we can see that the dark and bright ice was formed in what seems to be different time periods. The pores that froze in the first 6-7 hours froze water that becomes a dark ice as shown in figure 4.15. From approximately 7 to 17 hours, the ice matured to become bright in the images as in figure 4.16. The plot does not include the effects observed after thawing, but qualitatively, all pores that were frozen cavitated in less than a minute after thawing. Data on thawing in hydrogel will be presented in the next section.

If we consider the driving force of freezing as the degree of undercooling, ΔT,

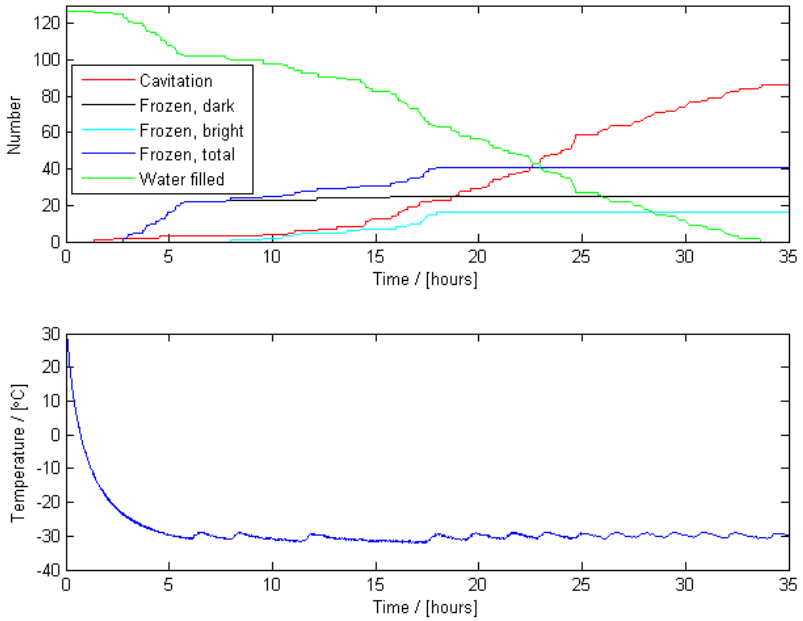

Figure 4.17: The upper plot shows the number of cavitated, frozen and water filled pores through time. The corresponding temperature has been plotted below.

the probability of freezing should not be time dependent, but rather

$$P_f(\Delta T) \propto \alpha' \tag{4.2}$$

where α' is a constant. If this is the case, the freezing rate should be on the form

$$\frac{\partial N_f}{\partial t} = k_f P_f(\Delta T) N_w = \alpha N_w \tag{4.3}$$

where N_w is the number of remaining water filled pores and k_f is a rate constant that has been absorbed into α. Integrating both sides leaves us with the expression

$$N_f = \alpha N_w t \tag{4.4}$$

Figure 4.18(a) shows a plot of N_f as a function of $N_w t$. To comply with the assumption of constant ΔT, the data used in the analysis was taken from the period between 5 and 35 hours (figure 4.17). If this simple model accurately describes the behavior of the freezing pores in the hydrogel sample, the plot should yield a straight line with slope α. What we observe is that this model does not describe the behavior of the freezing rate for this system.

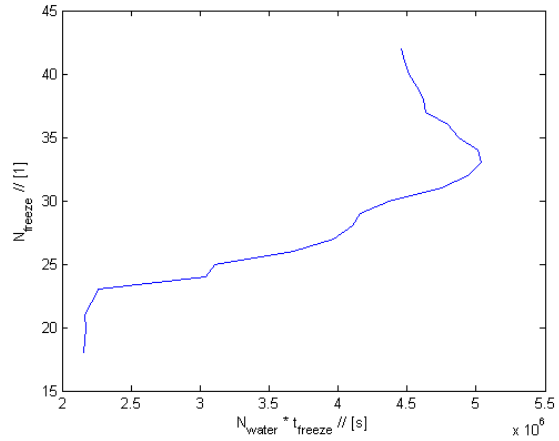

(a) Plot of number of frozen pores as a function of the number of remaining pores with water.

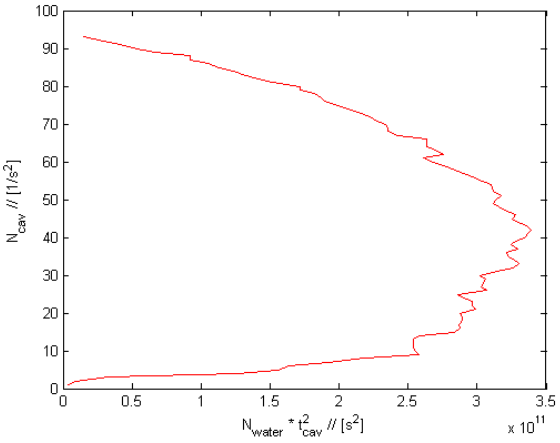

(b) Plot of number of cavitated pores as a function of the number of remaining pores with water.

Figure 4.18: The figures show plots where the number of cavitated and frozen pores have been plotted against the number of pores that remain with liquid water with different scaling. Data collected from experiment 120529 (table 4.1).

A similar analysis was conducted of the scaling that governs the cavitation rate. For this case, the driving force is the pressure (or tension), p. If we assume that the evaporation is constant, the probability of cavitation should go as

$$P_c(p) \propto t \tag{4.5}$$

Given this, the cavitation rate can be written as

$$\frac{\partial N_c}{\partial t} = k_w P_c(p) N_w = \beta' N_w t \tag{4.6}$$

where the rate constant k_w has been absorbed into β'. The expression for the number of cavitated pores is found by integrating both sides, which yields

$$N_c = \beta N_w t^2 \tag{4.7}$$

where $\beta = \frac{\beta'}{2}$. N_c versus $N_w t^2$ is plotted in figure 4.18(b). Again, the system does not display a linear behavior with this scaling. This tells us that the simple model proposed here does not describe the cavitation process observed in the hydrogel sample.

4.2.2 Thawing

On thawing in the hydrogel sample, two modes of thawing were observed. In both modes, cavitation happend during thawing, i.e. before the ice was completely melted. One mode demonstrated nucleation of water in the pore that eventually cavitated as before. This is shown in figure 4.19, were we initially had a pore filled with ice (figure 4.19(a)). One second later, thawing was observed to begin (figure 4.19(b)), and after 3.5 seconds a gas bubble had nucleated and started to grow (figure 4.19(c)). Figure 4.19(d) shows the bubble after 40.5 seconds. The pore was completely dry after a total of 106.5 seconds.

The other mode of thawing is shown in figure 4.20, where we observed three pores that thawed simultaniously. The first image (figure 4.20(a)) shows the three diagonally placed pores (top left to bottom right) with stable and matured ice. Figure 4.20(b) shows the pores in the early stage of thawing. We notice that the ice had become less bright in the image and more transparent. This was observed by the outline of the pore wall through the ice. On the third image, figure 4.20(c), the ice had clearly lost volume, but there was still no sign of the typical meniscus we saw in figure 4.19. The ice continued to decrease in volume, and figure 4.20(d) shows that the central pore was now empty and dry while there was still some residue of ice in the neighbouring pores. The key observation was that none of the pores displayed a meniscus, which is commonly associated with a liquid-gas interface. This was what separates the two modes of thawing.

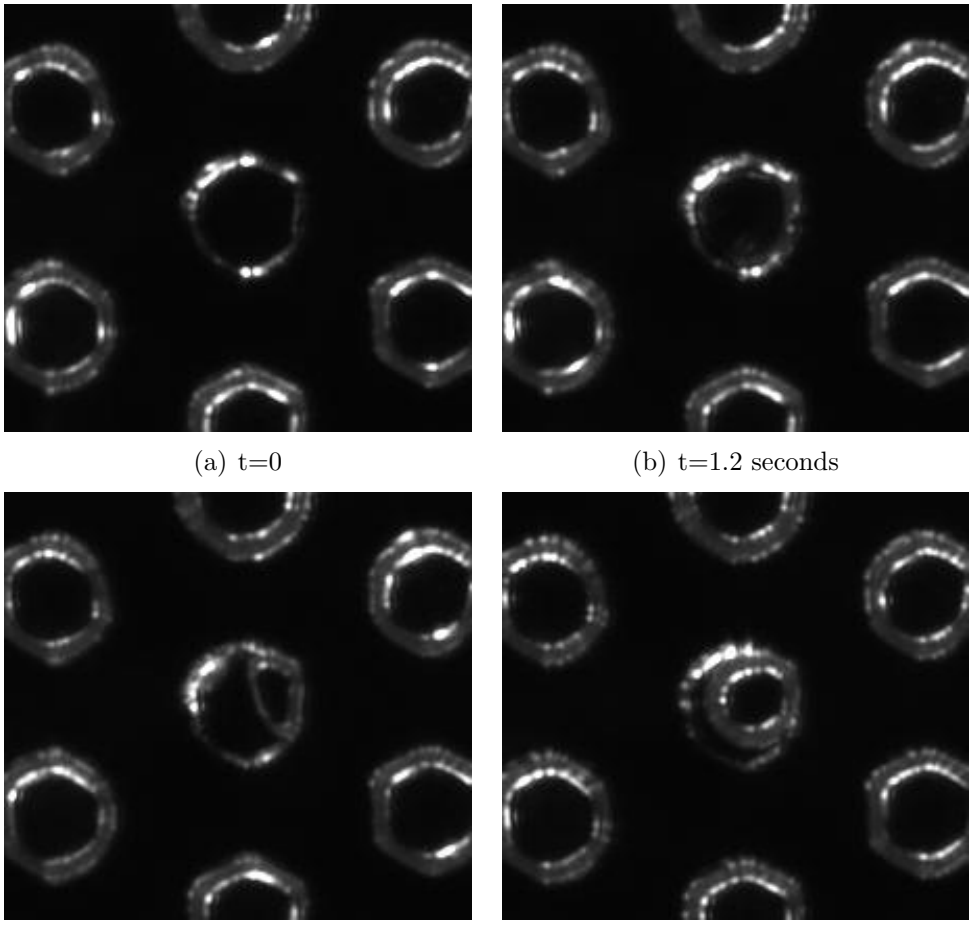

(a) t=0 (b) t=1.2 seconds

(c) t=3.5 (d) t=40.5 seconds

Figure 4.19: The pictures show cavitation on thawing of ice in the center pore. As a comparison, the surrounding pores are already cavitated and dry. Note the slightly thicker and brighter rim of the surrounding pores compared to the one in the center (a). The images are taken of the hydrogel sample from experiment 120529 (table 4.1) where the pores have a radius of 50μm.

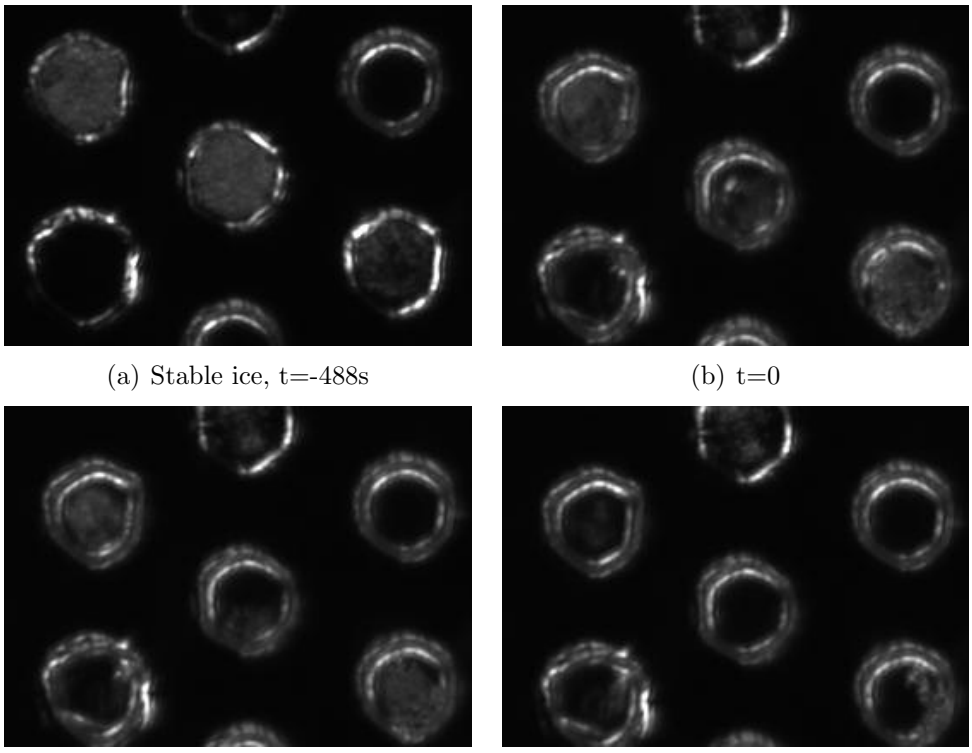

(a) Stable ice, t=-488s (b) t=0

(c) t=17s (d) t=36s

Figure 4.20: The pictures show thawing of ice in three pores where there is no apparant liquid state. The images are taken of the hydrogel sample from experiment 120529 (table 4.1) where the pores have a radius of 50μm. Note, it was difficult to establish the time of the onset of thawing, so the times listed are only estimates.

Chapter 5

Discussion

This chapter will discuss the main observations of the experiments and it has been divided into three main sections. The first section will discuss the observations made on freezing in the different system types. They were

- two-stage freezing in pore networks and capillary tubes
- The effect of connected pores versus isolated pores

The second section will deal with the observations of thawing and release of bubbles in the systems studied. It will focus on the observations of

- the uniform size distribution of bubbles in PDMS
- the redissolution of bubbles
- the release of bubbles over several cycles

The third and last section will focus on the observed cavitation in the hydrogel sample and the drying process in the PDMS samples. The discussion will go through the main observations that were

- the scaling of the cavitation rate in the hydrogel sample
- the drying and expansion of gas in the PDMS samples
- the pinch-off effect observed in the pore network

The mechanisms that control the processes and the implications for natural systems will be discussed in each section. In addition, some ideas for experiments that might shed some light on the processes will be mentioned.

5.1 Freezing

5.1.1 Two-stage freezing

In all systems studied we observed a degree of undercooling before the system froze, which in the PDMS and capillary samples, was a two-stage process. It began as a rapid spread of ice that appeared brighter on the pictures than the following stable ice, as described in section 4.1.1. After the first wave of ice, a slower growth of stable ice was observed.

The apparent brightness of the first ice in two-stage freezing

The first ice formed in the pores of the PDMS did not appear to be dendritic in the same manner as seen in the capillary tube. However, the fact that the ice appeared so bright in the images indicate that it was made up of either small crystals or a dendritic pattern that was too fine to be picked up by the cameras resolution. In either case, the brightness was most likely caused by the large area of refracting or reflecting surfaces during the first stage of freezing.

The subsequent decrease in intensity in the images can be explained by the rounding off of either the small crystals or the dendritic needles. This could have happened either by ice growing on the flat surfaces or melting of the edges. The latter was possible due to the raised temperature from the release of latent heat, possibly aided by local temperature fluctuations. Of the two, the melting scenario seems the most probable, as growing crystals on flat surfaces is a slow and energetically expensive process. The rounding off of the ice crystals or needles caused a smaller fraction of the total surface to have the needed orientation to redirect the light into the lens. This could explain the rapid darkening of the first wave of ice.

Another possible explanation of the observations is that when the front of the first wave of ice grew, numerous small bubbles were pushed in front of the ice due to the low solubility of gas in ice (about one thousand times smaller than in water, Morris and McGrath [1981]). The bubble surfaces, possibly aided by the ice, could redirect the light towards the lens and thus cause the intensities observed. Given that the ice did not trap the small bubbles, they could have redissolved rather quickly (figure 4.8), thus explaining the loss of intensity before the stable ice was formed.

The duration of the first stage in two-stage freezing

In the capillary tube experiment we observed that the first stage of ice did not fill the intire volume of the tube. This is explained by the release of latent heat. When the system froze and latent heat was released, the temperature of the water surrounding the ice was raised to 0°C. Note that the temperature could not be raised further because if it had, ice would no longer be the energetically favoured phase.

If we look at the properties of water, we know that the latent heat of fusion of water is $L = 334\frac{kJ}{kg}$ and the specific heat at 25°C is $C_p = 4.18\frac{kJ}{kgK}$ [Robert C. Weast, 1984]. At the onset of freezing at an undercooling of approximately $\Delta T = 13$°C, the ratio of frozen to unfrozen volume should be given as

$$\frac{V_{ice}}{V_{water}} = \frac{\Delta T C_p}{L} = 0.163 \approx \frac{1}{6} \tag{5.1}$$

This means that before heat is removed, only a sixth of the system will have frozen before the temperature of water reaches 0°C, regardless of the initial volume of water. This indicates that the fraction of frozen water in the capillary tube and in the PDMS samples in the first stage of freezing were approximately the same. Note that this ignores any volume or pressure changes in the system due to phase change.

The first stage of freezing can thus be described by the rapid growth of ice until the latent heat has increased the temperature to 0°C. But what controls the duration of this process? In the analysis we found that τ_1 was 0.28 and 0.29 seconds for the PDMS systems with 300 and 3000 pores respectively. However, the measurement on capillary tube experiment yielded $\tau_1 = 9.0$ seconds. The obvious difference between the two systems was that the total amount of ice in the capillary tube was far greater than that of the two PDMS systems. However, the similar τ_1 of the PDMS systems indicate that an approximate change in volume of a factor ten did not affect the parameter. Still, the measurements of τ_1 for the PDMS systems were most likely subject to a large degree of uncertainty since the number of measurements were highly limited by the temporal resolution of the pictures.

Another possible factor to consider is the degree of undercooling. If the driving force behind the initial formation of ice is the energy difference between the liquid and frozen state, the degree of undercooling might be a factor influencing the initial growth rate of the first stage of freezing. However, it should not affect the the apparent darkening of the ice because this most likely happens after the temperature has been raised to 0°C. To determine

whether the total volume is the controlling parameter and the effect of undercooling, a detailed study of capillary tubes, or pore networks in PDMS, of varying sizes could be conducted with a sufficiently high time resolution. To control the degree of undercooling, it might be possible to systematically control the impurity concentration with the use of destilled water and silver iodide.

The formation of stable ice in two-stage freezing

As discussed in the previous section, the temperature of the water in a freezing system is raised by the release of latent heat. If the water in the system reaches 0°C, further growth of ice is limited by the thermal conductive properties of the system. The growth rate of the stable ice observed in the experiments was thus believed to be controlled by the conduction of latent heat, i.e. the rate of cooling of the water that was heated to 0°C. This is consistent with the findings of Sun and Scherer [2010] who determined that the heat conduction properties of a system greatly influenced the growth rate of ice, namely that greater heat conduction yielded higher growth rates.

Qualitatively, this could explain the time difference of the process in the case of the pore network in PDMS, shown in figures 4.1 and 4.3, to the capillary tube, shown in figure 4.5. In the former case, the bulk volume of water was small and the block of PDMS could function as a reservoir. In addition, the water and ice in the pores were in direct contact with the relatively thick glass slide (1mm thick). The capillary tube had a much higher bulk volume and it is made up of much thinner glass than the glass slide in the PDMS system. Note, the thermal contact between the capillary tube and the glass slide it was mounted on was most likely not good. An additional consideration is that the volume of water in the PDMS network had a higher surface to volume ratio than that of the capillary tube. These factors would make the latter system less thermally conductive and the process should be slower. This was reflected in the measurements of the characteristic time τ_2, where the paramter was 2-3 times larger for the capillary tube ($\tau_2 = 12.55$) compared to the two PDMS systems. The bulk volume was also seen to have an effect between the two PDMS systems, where the sample with 300 pores had a $\tau_2 = 3.25$ seconds and the system with 3000 pores had $\tau_2 = 5.09$ seconds.

Two-stage freezing was not observed in the experiments with hydrogel due to the difficulty of predicting when the pores would freeze. Given that it occured and that conduction of latent heat was what controlled the growth

rate of the stable ice, one would expect the growth of the ice in the pores in hydrogel to be approximately as fast as in the PDMS network. This is based on the comparable volumes of water and surface to volume ratio. However, a major difference between the two systems was that in the pore network in PDMS, all the water froze at the same time whereas in the hydrogel, individual pores froze over many hours. This means that the PDMS system had a much higher production of latent heat per time on freezing than the hydrogel system. This could mean that the growth rate of stable ice in the isolated pores in the hydrogel was faster. An additional observation is that growth rate in hydrogel might be slowed down compared to the PDMS due to the fact that the water in the hydrogel is not in direct contact with glass. This means that the rate is probably determined by the thermal properties of the hydrogel. To further study two stage freezing and confirm that it does occur for small isolated pores, a similar set up with a higher time resolution could be used.

5.1.2 General behavior of the network & indications

The fact that the pore networks in the PDMS experiments froze from pore to pore indicated that the ice nucleated in one pore and grew into the next pores rather than the isolated nucleation events observed in the hydrogel experiments. What the observations in this thesis show is that for a single pore, the ice grows by seeding of an intruding ice crystal, see figure 4.7. This indicates that the freezing of a tracheid network in the xylem of trees could occur in a similar manner, i.e. from ice nucleating in one tracheid which grows and seeds neighbouring tracheids.

The question is then, would pit openings that connect individual tracheids allow a crystal to grow through them? If we can consider the pit opening as an open hole between the cells, the question should be answered by whether the crystals have sufficient driving force to grow crystal shapes with a high enough curvature [Scherer, 1993]. Alternatively, if the first wave of ice that is formed in the pores is dendritic, the ice is already out of equilibrium and could have a size and curvature which allow the needles to grow through the pit openings. This ice would then be sufficient to seed the volumes of water inside the tracheids they grow into, as observed in the PDMS experiments presented in this thesis. In this case, the question should be answered by the size of the dendritic needles in the system.

If either of these ideas are correct, a single nucleation event could be enough to crystallize much, if not all, of the water in the tracheid network. In the

experiments of Mayr and Sperry [2010], they observed exotherms in tree segments at about -6°C that were interpreted as freezing events. If one exotherm for one sample indicates that the intire network has frozen, it could indicate that the natural networks freeze in a similar manner as observed in the PDMS samples. Possible ways to investigate this further could be by using an infrared camera on actual tree samples to observe the release of latent heat over time and possibly creating similar microfluidic systems as those presented in this thesis with more realistic dimensions and geometries.

Crude measurements of some of the dendritic needles from figure 4.5, indicate that they can be in the order of tens of microns in bredth in this system. However, given that the dendritic ice is formed in the first stage of freezing, we have that

$$\frac{V_{ice,dendritic}}{V_{water}} \approx \frac{1}{6} \tag{5.2}$$

which means that the size of the dendritic needles is scaled by the size of the system. If dendritic ice exists in tracheids, the size of the needles could be comparable to the pore opening. If we compare the size ratio of the capillary tube and its dendritic needles to the size of a tracheid, it might suggest the possibility that the needles are in the order of microns. However, the measurements of the dendritic needles observed in the experiment were limited by the resolution of the images. This could be studied further by applying higher resolution imaging to try and find a scaling to the size of the dendritic needles in capillary tubes of varying sizes.

The observed freezing rate in the hydrogel experiment was considerably slower than that of the PDMS. However, the simple model proposed in the scaling analysis did not prove to describe the system accurately. This led us to believe that a more complex behavior of the freezing probability than the one that was proposed, namely that the probability was constant given a constant degree of undercooling.

5.2 Thawing, release of bubbles

Observations made on thawing in the PDMS experiments (figure 4.8) show that the bubbles that were trapped in the ice of the pore network were uniformly distributed in the pore. This might indicate that the ice grew fast enough to enveolp and trap the bubbles. Another behavior was observed in one of the capillary experiments (figure 4.11). The band of bubbles that were observed were most likely pushed in front of the ice as it grew. This requires

the ice to grow slowly enough such that the ice does not grow around the bubbles. The position of the bubbles was consistent with ice growing from the sides while pushing the gas bubbles in front of it. This made the bubbles coalesce, creating large bubbles that were distributed locally where the last ice formed. The reason for the unsymmetrical position of the band, was gravity. As the bubbles were frozen out, the ones from the lower freezing front drifted upwards, hindering the upper front from having access to equal amounts of water. Thus, the ice created in the lower front had more available water and a larger volume to grow in.

If the difference between these behaviors was the freezing rate, one would expect that the behavior and size of the bubbles formed in trees is determined by the heat conducting properties of the tracheid matrix and surrouding tissue. This could be studied with a similar setup as used here by studying bubble distribution inside capillary tubes that froze with different rates, i.e. in systems with different thermal conductive properties. The thermal conduction could be controlled by systematically isolating the system or putting it in contact with a thermal reservoir.

Also, one of the questions posed at the beginning of this thesis was if gas was forced was out of solution over several cycles or if it all was separated out during the first cycle. What was observed was that bubbles did indeed separate out on all cycles where the background noise allowed for their observation. However, the water in the PDMS networks, and certainly the water in the capillary tubes, were not subject to as low pressures as observed in nature. The pressure in the experiments might have lead to a higher amount of gas being redissolved after thawing which could be frozen out on the subsequent cycles. In the PDMS networks, no observable stable bubbles were observed after thawing indicating that most, or all, bubbles released on thawing were redissolved. In the capillary tube (experiment 120119), a stable bubble was observed to grow over four cycles. However, some bubbles redissolved and it is likely that it was that volume of gas which was observed to be separated out on the next cycle. The growth of the stable bubble in this system might then simply be the effect of bubbles randomly being close enough to coalesce with this bubble before redissolving.

So how does the volume of the bubbles in figure 4.10 compare to those that would be expected at 1atm pressure? Morris and McGrath [1981] reported that the solubility of air in ice is at least one thousand times less than the solubility of air in water. If we calculate the amount of dissolved gas of water at 1atm and 25°C and imagine that all of this is separated out in a capillary tube, the amount of gas present in the capillary tube would cover an area

of approximately 7mm^2 (Henry's law, constants taken from Atkins [1978]). Given that the seals were pushed out on freezing and stayed in place on thawing, it is not unlikely that there is also slightly lowered pressure in the gas which might stretch the bubbles. With this in mind, and using the height of the capillary tube for scale (4mm), the bubble present in figure 4.10(d) is not unreasonable. The enviroment in the capillary tube was thus considered to not be far from 1atm pressure.

The fact that stable bubbles was present in the capillary system prove that the amount of bubbles separated out on thawing was large enough, due to the large volume of water, to form stable bubbles. This is contrary to the observations done when using PDMS where all bubbles redissolved, indicating that there might be some critical volume of water in which stable bubbles can be formed and that the two systems were on either side of that threshold. If this is not the case, the PDMS matrix may also have resisted the volume change when gas was forced out, leading to an increased pressure which forced the bubbles to redissolve. Note, this is given that the evaporation observed has not considerably lowered the pressure in the pore network.

As stated above, we observed that bubbles redissolved, sometimes within seconds. If the ice in a thawing tracheid cell protects the bubbles from experiencing the tension of the water, the bubbles that would normally be large enough to cavitate might redissolve in local and isoltaed pockets of undersaturated water before to being subject to it. This dissolved gas can be frozen out and cause an ebolism on subsequent cycles.

If we imagine the tracheid cells as being long cylinders connected with thin channels, a cross section would look much like figure 3.2(a). According to the Gibbs-Thompson equation (equation 2.38), a crystal that has been forced to take on a higher curvature will have a lower melting point, i.e. it will melt sooner than the ice in the pore. For a system like described above, this means that the ice in the channels would be the first to melt. As opposed to freezing, melting requires latent heat which essentially would lower, or at least keep, the temperature around the channel opening to the pore at the melting temperature of the ice in the channel for a while before all the ice is gone from the channel. If the ice in the pore that is not close to the channel opening has a slightly higher local temperature and starts to melt before the ice at the channel opening, the water produced in the pore is essentially isolated from a stable column of water and thus isolated from experiencing tension. This might, in some cases, allow the gas to redissolve in the undersaturated and isolated volume of water before it can embolize. If this is the case, thawing rates and the thermal conductivity of the system should be contributing

factors to the embolism rates. Specifically, an increased thawing rate should increase the chance of embolisms. This might be a mechanism involved to explain why multiple freeze-thaw cycles induce more embolisms. A possible way to study the temperature distribution on thawing could be by using infrared imaging in a setup similar to the one used in these experiments.

5.3 Drying & cavitation

Cavitation in hydrogel

In the hydrogel experiments, two modes of cavitation after thawing were observed, one where a gas bubble clearly expanded and one where no meniscus was observed. The latter might have been that the volume of liquid water that cavitated was covered by a film of ice on the surface. Another possible explanation is that the volume of water was seeded by the release of small gas bubbles from the ice and thus cavitated immidiately after a bubble came in contact with liquid water. This could account for the observations made.

A third possibility is that the ice undergoes a second order phase change, i.e. going from solid ice to water vapor without passing through the liquid phase. This seems somewhat less likely because the two modes of cavitation on thawing happened at the same temperatures. That would indicate that the ice reached the melting temperature before undergoing the second order phase change.

Vincent et al. [2012] conducted experiments on hydrogel samples of similar size (pores with approximately 50μm diameter) and reported that the pressure at which cavitation occured was measured to be 30$\pm$16MPa. Also, they stated that similar systems had measured cavitation pressures of 22MPa for systems similar to those they were using. However, as the scaling analysis presented in this thesis showed, the observed cavitation rate was not explained by a model where one assumes that the cavitation probability is linear with time.

Drying of PDMS

The drying observed in the experiments with PDMS was most likely due to gas that was already present at the injection site. This volume of gas was expanded by a lowered pressure in the pore network created by evaporation

from a surface of the PDMS (the specific surface was not determined). The expansion of gas relaxed the pressure, thus allowing more water to diffuse out and continue the extension of the gas. On filling, the pressure in the network was 1atm. When the small volume of gas at the injection site was expanded, the pressure could eventually reach the vapor pressure of water. The expansion of the gas volume would then be from evaporation of the liquid water. If this was the case, the pressure when the pore network dried should eventually approach $p = 0$atm. However, any negative pressure in the system after a volume of gas was present was not likely as the gas would either expand or water would vaporize. This resulted in drying of the system without it being subject to negative pressure which, in turn, indicated that the PDMS systems were not subject to cavitation.

The idea that there was a small volume of gas present at the injection site was corroborated by the fact that the gas volume seemed to stretch from the upper left, which was the position of one of the injection sites (figure 4.12(a)). The reason why it did not also dry from the other injection site at the bottom right might be that the volume of gas present in the upper left injection site was slightly bigger and thus easier to stretch. Once one of the volumes of gas relaxed the pressure there was no additional pressure difference to expand the other gas volume. However, if gas was present at the other injection site, one would expect that volume to expand prior to the system reaching the vapor pressure of water. This was not observed, thus indicating that the pressure in the pore network did not reach the vapor pressure of the water. Note, figure 4.12(d) shows a volume of gas in the bottom right corner. This was confirmed to be part of the connected volume of gas present and thus interpreted not to be a second isolated volume of gas.

The observation of small bubbles that formed when a pore dried (figure 4.13) has been interpreted as the result of a pinch-off effect by the channel opening [Dollet et al., 2008]. This is typically observed in microfluidic systems where one has continuous flow through a choke point.

Chapter 6

Conclusion

The observations of freezing in undercooled systems have led us to conclude that it is a two-stage process. The first stage is the nucleation and rapid growth of ice which grows until the remaining water in the system is heated to approximately 0°C. This ice, which is possibly dendritic, has a high surface to volume ratio, which would explain the apparent brightness in the images. The second stage is the growth of ice where the rate is determined by the heat conduction properties of the system. This ice, which eventually becomes stable, was less bright in the images, which led us to conclude that the ice in the second stage of freezing has a lower surface to volume ratio than the first.

The possibility of a role of dendritic ice in the freezing of a network and implications to natural systems were discussed. Further analysis and insight into the freezing process of pore networks could prove helpful when studying frost damage in trees. The method developed allowed for the possibility of a wide variety of pore network geometries, and studying geometries specifically designed to mimic those found in tracheid networks could prove helpful. Another possibility is to use the hydrogel, but instead of having uniformly sized pores or connected pores, one could have isolated pores with varying size. That way, a scaling for the probability of cavitation as a function of pore size could be found. This might aid in understanding cavitation in tracheids of varying size.

Two distinct behaviors were observed on thawing. In the case of the PDMS experiments, the bubbles released on thawing were uniformly distributed. In the case of a capillary experiment, the growth rate was most likely slow enough to push the bubbles in front of the growing ice. If the growth rate of

the ice is what determines the behavior, the thermal conductive properties of the system could prove to be a key factor to the size of the bubbles released on thawing. This has led us to conclude that the heat conducting properties of the tracheid matrix and the surrounding tissue might be a contributing factor to the embolism rates in trees.

Bibliography

P. W. Atkins. *Physical Chemistry*. University Press, Oxford, Oxford, Great Britain, 1978.

J. Crank. *The mathematics of diffusion*. Clarendon Press, Oxford, 2nd edition edition, 1979.

Benjamin Dollet, Wim van Hoeve, Jan-Paul Raven, Philippe Marmottant, and Michel Versluis. Role of the channel geometry on the bubble pinch-off in flow-focusing devices. *Physical Review Letters*, 100(3):034504, 2008. PRL.

Jens Feder. *Flow in Porous Media*, chapter Chapter 10: Capillary Action, pages 107–124. 1996.

U. G. Hacke and J. S. Sperry. Functional and ecological xylem anatomy. *Perspectives in Plant Ecology Evolution and Systematics*, 4(2):97–115, 2001.

K. F. Kelton. *Crystal Nucleation in Liquids and Glasses*, volume 45. Harcourt Brace Jovanovich, Publishers, Harvard University, Cambridge, Massachusetts, 1991.

Antonio C. Lasaga. *Kinetic Theory in the Earth Sciences*. Princeton series in geochemistry. Princeton University Press, New Jersey, USA, 1998.

S. Mayr and J. S. Sperry. Freeze-thaw-induced embolism in pinus contorta: centrifuge experiments validate the 'thaw-expansion hypothesis' but conflict with ultrasonic emission data. *New Phytologist*, 185(4):1016–1024, 2010. Mayr, Stefan Sperry, John S.

S. Mayr, A. Gruber, and H. Bauer. Repeated freeze-thaw cycles induce embolism in drought stressed conifers (norway spruce, stone pine). *Planta*, 217(3):436–441, 2003. Mayr, S Gruber, A Bauer, H.

G. J. Morris and J. J. McGrath. Intracellular ice nucleation and gas bubble formation in spirogyra. *Cryo-Letters*, 2(NOV):341–&, 1981.

J. W. Mullin. *Crystallization*. Butterworth-Heinemann, Oxford, fourth edition, 2001.

P. Marmottant O. Vincent. Cavitation in a confined liquid equilibrium states and bubble dynamics (preprint). 2012.

Greg C. Randall and Patrick S. Doyle. Permeation-driven flow in poly(dimethylsiloxane) microfluidic devices. *Proceedings of the National Academy of Sciences of the United States of America*, 102(31):10813–10818, 2005.

Melvin J. Astle Robert C. Weast. *CRC Handbook of Chemistry and Physics*. CRC Press, Boca Raton, Florida, USA, 63 edition, 1984.

G. W. Scherer. Freezing gels. *Journal of Non-Crystalline Solids*, 155(1):1–25, 1993.

Z. H. Sun and G. W. Scherer. Measurement and simulation of dendritic growth of ice in cement paste. *Cement and Concrete Research*, 40(9): 1393–1402, 2010.

William A. Tiller. *Chapter 8: General kinetics and the nucleation process*, chapter 8, pages 327–381. Great Britain, Cambridge, 1991.

Olivier Vincent, Philippe Marmottant, Pedro A. Quinto-Su, and Claus-Dieter Ohl. Birth and growth of cavitation bubbles within water under tension confined in a simple synthetic tree. *Physical Review Letters*, 108(18): 184502, 2012. PRL.

J. M. Watson and M. G. Baron. The behaviour of water in poly(dimethylsiloxane). *Journal of Membrane Science*, 110(1):47–57, 1996.

T. D. Wheeler and A. D. Stroock. The transpiration of water at negative pressures in a synthetic tree. *Nature*, 455(7210):208–212, 2008.